NASA/TM—2000-210027

A New Local Failure Model With Application to the Longitudinal Tensile Behavior of Continuously Reinforced Titanium Composites

Brett A. Bednarcyk
Ohio Aerospace Institute, Brook Park, Ohio

Steven M. Arnold
Glenn Research Center, Cleveland, Ohio

May 2000

The NASA STI Program Office . . . in Profile

Since its founding, NASA has been dedicated to the advancement of aeronautics and space science. The NASA Scientific and Technical Information (STI) Program Office plays a key part in helping NASA maintain this important role.

The NASA STI Program Office is operated by Langley Research Center, the Lead Center for NASA's scientific and technical information. The NASA STI Program Office provides access to the NASA STI Database, the largest collection of aeronautical and space science STI in the world. The Program Office is also NASA's institutional mechanism for disseminating the results of its research and development activities. These results are published by NASA in the NASA STI Report Series, which includes the following report types:

- TECHNICAL PUBLICATION. Reports of completed research or a major significant phase of research that present the results of NASA programs and include extensive data or theoretical analysis. Includes compilations of significant scientific and technical data and information deemed to be of continuing reference value. NASA's counterpart of peer-reviewed formal professional papers but has less stringent limitations on manuscript length and extent of graphic presentations.

- TECHNICAL MEMORANDUM. Scientific and technical findings that are preliminary or of specialized interest, e.g., quick release reports, working papers, and bibliographies that contain minimal annotation. Does not contain extensive analysis.

- CONTRACTOR REPORT. Scientific and technical findings by NASA-sponsored contractors and grantees.

- CONFERENCE PUBLICATION. Collected papers from scientific and technical conferences, symposia, seminars, or other meetings sponsored or cosponsored by NASA.

- SPECIAL PUBLICATION. Scientific, technical, or historical information from NASA programs, projects, and missions, often concerned with subjects having substantial public interest.

- TECHNICAL TRANSLATION. English-language translations of foreign scientific and technical material pertinent to NASA's mission.

Specialized services that complement the STI Program Office's diverse offerings include creating custom thesauri, building customized data bases, organizing and publishing research results . . . even providing videos.

For more information about the NASA STI Program Office, see the following:

- Access the NASA STI Program Home Page at ***http://www.sti.nasa.gov***

- E-mail your question via the Internet to help@sti.nasa.gov

- Fax your question to the NASA Access Help Desk at (301) 621-0134

- Telephone the NASA Access Help Desk at (301) 621-0390

- Write to:
  NASA Access Help Desk
  NASA Center for AeroSpace Information
  7121 Standard Drive
  Hanover, MD 21076

NASA/TM—2000-210027

A New Local Failure Model With Application to the Longitudinal Tensile Behavior of Continuously Reinforced Titanium Composites

Brett A. Bednarcyk
Ohio Aerospace Institute, Brook Park, Ohio

Steven M. Arnold
Glenn Research Center, Cleveland, Ohio

National Aeronautics and
Space Administration

Glenn Research Center

May 2000

Acknowledgments

The authors wish to thank Dr. Jacob Aboudi of Tel Aviv University for several fruitful discussions regarding this investigation. In addition, we thank Dr. Cheryl L. Bowman and Michael G. Castelli of the Ohio Aerospace Institute for providing data and expertise regarding the experimental results presented herein. This work was supported by NASA Contract NCC3-650.

Trade names or manufacturers' names are used in this report for identification only. This usage does not constitute an official endorsement, either expressed or implied, by the National Aeronautics and Space Administration.

Available from

NASA Center for Aerospace Information
7121 Standard Drive
Hanover, MD 21076
Price Code: A03

National Technical Information Service
5285 Port Royal Road
Springfield, VA 22100
Price Code: A03

A New Local Failure Model with Application to the Longitudinal Tensile Behavior of Continuously Reinforced Titanium Composites

Brett A. Bednarcyk
National Aeronautics and Space Administration
Glenn Research Center
Cleveland, Ohio 44135

Steven M. Arnold
Ohio Aerospace Institute
Brook Park, Ohio 44142

Abstract

A new model for local fiber failures in composite materials loaded longitudinally is presented. In developing the model, the goal was to account for the effects of fiber breakage on the global response of a composite in a relatively simple and efficient manner. Towards this end, the model includes the important feature of local stress unloading, even as global loading of the composite continues. The model has been incorporated into NASA Glenn's Micromechanics Analysis Code with Generalized Method of Cells (**MAC/GMC**) and was employed to simulate the longitudinal tensile deformation and failure behavior of several silicon carbide fiber/titanium matrix (SiC/Ti) composites. The model is shown to be quite realistic and capable of accurate predictions for various temperatures, fiber volume fractions, and fiber diameters. Furthermore, the new model compares favorably to Curtin's (1993) effective fiber breakage model, which has also been incorporated into **MAC/GMC**.

1. Introduction

Design and life prediction tools for advanced multi-phased materials are needed to facilitate the implementation of these developing materials. Although closure has not been reached regarding the best models for use in design and life prediction, it has become clear that if a model is ever to serve a purpose beyond that of basic research, it must fulfill several primary requirements. These include a significant level of accuracy on both the macro and micro scales, computational efficiency, and compatibility with the finite element method. Fulfillment of these requirements allows a model to serve the composite developer by enabling quick and easy variation of composite parameters for material development and optimization purposes. Likewise, those who attempt to utilize composites in structural design are well served if the model is consistent with the finite element method. Though it is not perfect, the generalized method of cells (**GMC**), originally developed by Aboudi (1991, 1995), is an excellent choice for implementation into modeling tools for advanced composites, given the requirements described above.

GMC is a fully analytical micromechanics model for multi-phased materials with arbitrary periodic microstructures. It provides pseudo closed-form multiaxial constitutive equations for such materials, and allows straightforward implementation of physically-based viscoplastic deformation models, as well as arbitrary failure and damage models for each phase. Further, recent independent advances have simplified the implementation of **GMC** as an elemental constituent material model in finite element analysis (Arnold et al, 1999), and significantly increased the model's computational efficiency (Pindera and Bednarcyk, 1999).

GMC has been implemented in the NASA Glenn Research Center developed comprehensive micromechanics analysis code, **MAC/GMC** (Arnold et al, 1999). The code has many features that render it useful for design, deformation modeling, and life prediction for a wide range of materials. These features include the ability to simulate general thermomechanical loading on composites whose geometries are represented by a library of continuous and discontinuous repeating unit cells, a library of nonisothermal elastic/viscoplastic constitutive models, fatigue damage analysis, yield surface analysis, laminate analysis, and interface modeling. The present investigation extends the capabilities of

MAC/GMC further by incorporating a new physically based micro-level failure model that allows local unloading of a given failed fiber to occur in the composite. The code, with its new capabilities, was employed to model the longitudinal tensile deformation and failure behavior SiC/Ti composites. The new debonding model, working in the context of the recently developed computationally efficient version of **GMC**, allows more accurate modeling of SiC/Ti composite behavior.

Because of SiC/Ti composites' excellent specific properties at elevated temperatures, these materials have been researched extensively over the last decade. Given continuous fiber reinforcement, the longitudinal deformation and failure behavior of these composites is dominated by the fiber when the fiber volume fraction is greater than approximately 20%, whereas, at lower fiber volume fractions, the failure behavior of the matrix phase becomes critical. Brindley and Draper (1993) characterized the longitudinal deformation and failure behavior of SiC/Ti-24Al-11Nb by three stages. The first stage is linearly elastic, while stage two begins with the onset of matrix yielding, which increases the compliance of the composite stress-strain curve. Stage three typically begins at approximately 0.6% global strain where individual fibers begin to fail. Finally, the composite fails as the matrix fractures along a path of fractured fibers. The details of this behavior can vary for different Ti matrix alloys, SiC fiber types, temperatures, strain rates, and fiber volume fractions. However, most researchers agree that the overall qualitative behavior remains consistent.

The local mechanisms that lead to the observed longitudinal deformation and failure behavior of SiC/Ti composites (and their relative importance) are less discernable. Clearly, when a fiber fails, (in the vicinity of the failure) the fiber can no longer support the stress that caused the failure. In this region, the stress is transferred to the matrix and nearby fibers and may lead to matrix damage or cracking, increased matrix deformation, and interfacial debonding or sliding. On this local microscopic level, the mechanics associated with the broken fiber are clearly complex. Various analyses have been conducted that explicitly account for some of these effects, examples of which are given below.

The chain-of-bundles approach (Harlow and Phoenix, 1978a,b; Stumpf and Schwartz, 1993) seeks to develop an expression for the probability of complete failure of a series (chain) of bundles of fibers based on the statistical failure probability of the individual fibers and the location of the each failure (along the fiber). When a fiber within a bundle fails in this approach, it can no longer support any stress, and, according to a local load sharing rule, the stress is redistributed to fibers that are close to the failed fiber. Since the failed fiber is also part of a chain (i.e., in series with another fiber), the chain-of-bundles approach also includes an "ineffective" length in the vicinity of the failure over which the stress supported by the fiber is reduced. With this model, a number of computationally demanding Monte Carlo type simulations must be performed to determine a probable strength for the composite.

Reifsnider and Highsmith (1982) modeled the longitudinal behavior of polymer matrix composites (PMCs) by considering an ellipsoidal fiber in the matrix material. These authors developed an expression for the longitudinal modulus of the composite based on the material properties of the constituents and the aspect ratio of the ellipsoidal fiber. Then, by decreasing the aspect ratio, they simulated breakage of the fiber into successively smaller sections. Results indicated that a noticeable reduction in composite stiffness would not occur until the fiber had fragmented into unrealistically small sections. Steif (1984) showed that more valid results were obtainable by including the effect of debonding at the fiber-matrix interface in the region of the fiber failure. Using a concentric cylinder model, this author found that shear-induced debonding could give rise to a larger ineffective length and reduce the longitudinal stiffness of PMCs considerably.

The well-known approach referred to herein as the Curtin model (Curtin, 1991, 1993) combines the statistical probability of fiber failure with a shear-lag approach to account for the ineffective length near a fiber failure. An expression for the stress in an effective fiber, which represents all fibers in the composite, is developed that includes the effect of broken or damaged fibers. A similar approach was combined with an elastic-plastic rule of mixtures to model the longitudinal deformation and failure of SiC/Ti composites by Weber et al (1994). Upper and lower bounds for the ultimate strength of the composite were determined by assuming no interaction and perfect alignment, respectively, of the fiber failures.

A finite element analysis of a composite containing broken fibers with fiber-matrix debonding near the fiber break was conducted by Nicholas and Ahmad (1994). These authors found that the length of the debond, as well as the size of the gap that constitutes the fiber break, has a significant effect on the longitudinal deformation of the composite.

The approach to modeling the longitudinal failure of composites taken herein is somewhat different. No attempt is made to account for the details of the micro-mechanisms associated with the tip of an actual broken fiber. **GMC**'s inherent lack of normal-shear coupling renders such an approach infeasible. Instead, the effects of these mechanisms on the global response of the composite are accounted for by allowing broken fibers to unload their stress. A **GMC** geometric representation of the composite containing many fibers can be employed, and as each fiber fails it unloads its stress to the remaining intact regions of the composite. The global effects of the micro-mechanisms are thus captured without explicitly modeling them. Hence, this fiber breakage model represents a very complex situation in a simplified manner (wherein lies its power), such that, in combination with the **GMC** approach, a computationally efficient, multiaxial, multiphase, constitutive model can be employed within a larger structural problem. This addresses the real purpose of micromechanics: to provide the response of a multi-phased material given the responses of the constituents, their geometric arrangement, and the loading on the material.

2. Micromechanics Model: The Generalized Method of Cells (GMC)

The geometry of the triply periodic version of **GMC** (**GMC-TP**) is shown in Fig. 1, wherein the microstructure of a periodic material is represented by a parallelepiped repeating unit cell consisting of an arbitrary number of parallelepiped subcells, each of which may be a distinct material. The method assumes a linear displacement field in each subcell and imposes continuity of traction and displacement components between subcells in an average sense (Aboudi, 1995). In the original formulation of the **GMC** equations, this procedure results in a set of linear equations,

$$\tilde{\mathbf{A}}\,\boldsymbol{\varepsilon}_s - \tilde{\mathbf{D}}\left(\boldsymbol{\varepsilon}_s^p + \boldsymbol{\alpha}_s \Delta T\right) = \mathbf{K}\,\bar{\boldsymbol{\varepsilon}}, \tag{1}$$

which are solved for a vector of all subcell strain components, $\boldsymbol{\varepsilon}_s$, to form strain concentration equations,

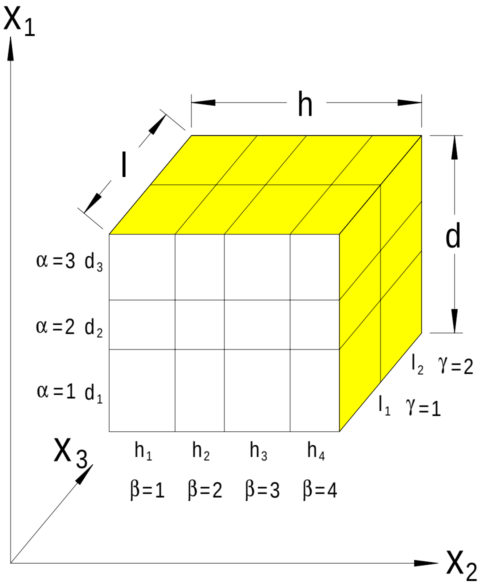

Fig. 1. **GMC-TP** repeating unit cell.

$$\boldsymbol{\varepsilon}_s = \mathbf{A}\,\bar{\boldsymbol{\varepsilon}} + \mathbf{D}\left(\boldsymbol{\varepsilon}_s^p + \boldsymbol{\alpha}_s \Delta T\right) \ . \tag{2}$$

Here, $\bar{\boldsymbol{\varepsilon}}$ is a vector of the global strain components, $\boldsymbol{\varepsilon}_s^p$ is a vector of all subcell inelastic strain components, $\boldsymbol{\alpha}_s$ is a vector of all subcell coefficients of thermal expansion (CTEs), and $\mathbf{A}$ and $\mathbf{D}$ are strain concentration matrices. Equation (2) provides expressions for the local (subcell) strains in terms of the global strains, local inelastic strains, and local CTEs; a characteristic that makes it a strain concentration equation. From this point, the global constitutive equations for the heterogeneous material can easily be formed by first employing the subcell constitutive equations to obtain the subcell stress components. Then, summations can be performed to obtain the global stress components in terms of the total, inelastic, and thermal strain components.

When implemented in a computer code such as **MAC/GMC**, the bulk of the computational effort associated with a given simulation is expended in solving eqn (1) for the unknown subcell strains. The number of equations represented by eqn (1) is, $6\ N_\alpha\ N_\beta\ N_\gamma$ where $N_\alpha,\ N_\beta,\ N_\gamma$ are the number of subcells in each of the three Cartesian coordinate directions (see Fig. 1). Thus, as the number of subcells within the repeating unit cell becomes large, a great deal of computational effort is required to determine the unknown subcell strain components. In addition, in the context of inelasticity and temperature-dependent constituent material properties, simulated loading (in the form of global stress or strain components) must be applied incrementally. Thus, solution for the subcell strains must occur not once, but typically thousands of times.

In order to increase the computational efficiency of **GMC**, a reformulation of the **GMC** equations has recently been performed by Pindera and Bednarcyk (1999) for the doubly periodic version, and by Bednarcyk and Pindera (2000) for **GMC-TP**. This reformulation takes advantage of the lack of shear coupling inherent to **GMC**, i.e., the constancy of certain stress components among certain subcells, to reduce significantly the number of unknowns for which solution is required. Consequently, instead of applying continuity of displacements and tractions in terms of the subcell *strain* components (as in the original formulation of **GMC**), these conditions are applied in terms of subcell *stresses*. The result is a mixed formulation in which only the unique subcell stress components are retained as unknown quantities.

In the reformulation, the following equation corresponds to eqn (1) from the original formulation of **GMC**:

$$\tilde{\mathbf{G}}\,\mathbf{T} = \mathbf{f}^{\mathbf{m}} - \mathbf{f}^{\mathbf{t}}\Delta T - \mathbf{f}^{\mathbf{p}} . \tag{3}$$

Here, $\mathbf{T}$ is the vector of all unique subcell stress components and $\mathbf{f}^{\mathbf{m}}$, $\mathbf{f}^{\mathbf{t}}$, and $\mathbf{f}^{\mathbf{p}}$ are vectors containing global total strains, subcell CTEs, and subcell inelastic strains, respectively. Solving eqn (3) for the unknown subcell stresses yields,

$$\mathbf{T} = \mathbf{G}\,\bar{\boldsymbol{\varepsilon}} + \boldsymbol{\Gamma}\,\Delta T + \boldsymbol{\Phi} , \tag{4}$$

where the inelastic and thermal terms are accounted for in $\boldsymbol{\Phi}$ and $\boldsymbol{\Gamma}$, respectively, and $\mathbf{G}$ is a mixed concentration matrix containing subcell dimensions and material compliance components. Equation (4) in the reformulated version of **GMC** replaces eqn (2) from the original formulation, and, as before, the global constitutive equations can easily be determined by performing summations of the subcell stress components (see Bednarcyk and Pindera, 2000).

Since in the reformulation we have retained only the unique subcell stress components, the number of unknown quantities (at each increment of the applied loading) is reduced to $N_\beta N_\gamma + N_\alpha N_\gamma + N_\alpha N_\beta + N_\alpha + N_\beta + N_\gamma$. For comparison, the number of unknowns versus the number of subcells, for both the original and reformulated versions of **GMC-TP**, is plotted in Fig. 2. Note, as the number of subcells in the repeating unit cell becomes large, the difference in the number of unknowns (and correspondingly computational speed) between the two versions becomes enormous. For example, in the case of a 10×10×10 unit cell, the reformulated version of **GMC-TP** has 330 unknowns while the original version has 6000. This reduction in the number of unknowns corresponds to a substantial increase in computational efficiency, as the inversion of a given matrix is on the order of the rank of the matrix cubed.

Table 1 compares CPU times for a sample **GMC** execution for a simulation of a heat-up of a SiC/TiAl composite. The table indicates the striking speed-up associated with the reformulation, particularly as the number of subcells becomes large. As demonstrated by Pindera and Bednarcyk (1999), the original formulation and reformulation of **GMC** yield identical results, thus the speed-up comes with no loss of accuracy. Clearly, utilization of the reformulation is crucial to the realization of reasonable execution times for application of **GMC** within the finite element analysis of structures.

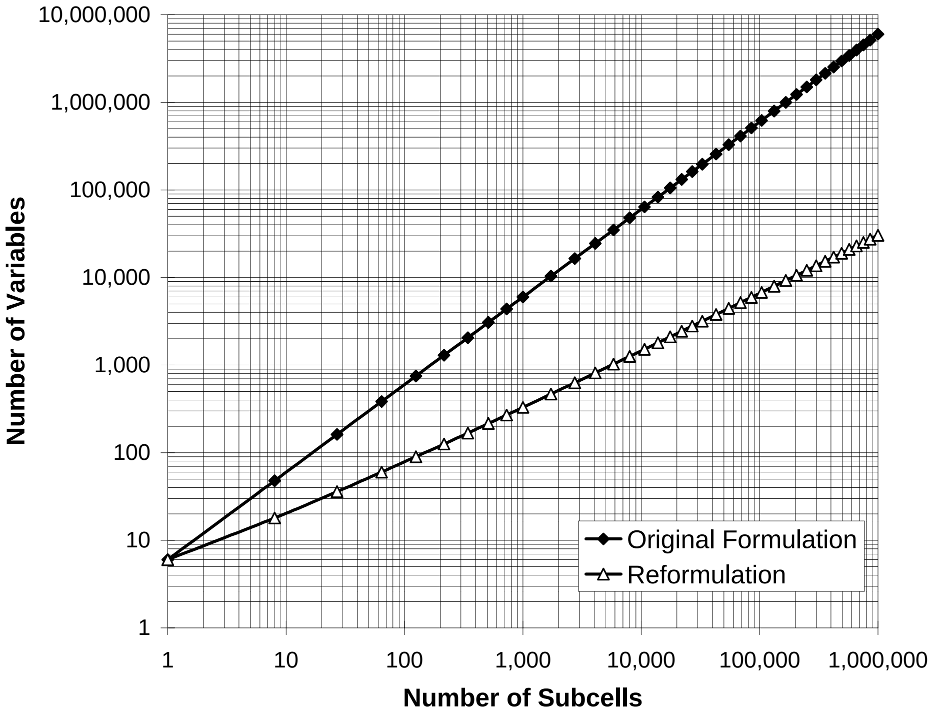

Fig. 2. Number of subcells vs. number of unknown variables for the original and reformulated versions of **GMC-TP** for $N_\alpha = N_\beta = N_\gamma$.

GMC Version	Subcell Discretization							
	2×2	4×4	6×6	8×8	10×10	12×12	20×20	100×100
original	0.87	19	182	508	8,679	43,781	-	-
reformulated	0.18	0.25	0.5	0.9	1.5	2.3	8.3	796
speed-up ratio	**4.8**	**76**	**364**	**563**	**5,786**	**19,035**	**-**	**-**

Table 1. CPU times (seconds) for a simulated heat-up of a unidirectional SiC/TiAl composite using a stand alone version of doubly periodic **GMC**.

3. Constituent Material Constitutive Models

For this study, the material analyzed is a metal matrix composite composed of continuous silicon carbide fibers (SCS-6 or SCS-9) embedded in a titanium alloy matrix, TIMETAL 21S[1].

3.1 Silicon Carbide Fibers

Textron's high-strength, high-stiffness, continuous SiC fibers are assumed in this study to be isotropic and linear elastic. The vendor-supplied temperature-dependent thermoelastic properties employed for the SCS-6 fiber are given in Table 2. Temperature-independent properties were employed for the SCS-9 fiber due to insufficient data. The vendor-supplied properties are as follows: E = 307 GPa, ν = 0.25, α = 4.3×10^{-6} °C^{-1}, where E is the elastic modulus, ν is the Poisson's ratio, and α is the coefficient of thermal expansion.

Temperature (°C)	E (GPa)	ν	α (1×10^{-6}/°C)
21	393	0.25	3.56
316	382	0.25	3.72
427	378	0.25	3.91
538	374	0.25	4.07
860	368	0.25	4.57

Table 2. SCS-6 fiber elastic properties.

3.2 TIMETAL 21S Matrix

TIMETAL 21S is a metastable beta strip titanium alloy, containing approximately 21% alloying additions, that has high strength as well as good creep and oxidation resistance. Consequently, TIMETAL 21S has been utilized in advanced metal matrix composites. Its (isotropic) viscoplastic response has been characterized for the model of Bodner and coworkers (Chan et al, 1988; Chan and Linholm, 1990) by Kroupa (1993), and Neu (1993), as well as for a generalized viscoplasticity with potential structure (**GVIPS**) model (Arnold and Saleeb, 1994) by Arnold et. al. (1996a,b). The **GVIPS** model of Arnold et. al. (1996a,b) has been employed in the current study. In this model, specific forms of both the Gibb's and complementary dissipation potentials are chosen such that a complete (i.e., fully associative) potential based multiaxial, nonisothermal, unified viscoplastic model is obtained. This model possesses a tensorial internal state variable that is associated with dislocation substructure, and an evolutionary law that has nonlinear kinematic hardening and both thermal and strain induced recovery mechanisms. A unique aspect of the **GVIPS** model is the inclusion of nonlinear hardening through the use of a compliance operator, derived from the Gibb's potential, in the evolution law for the back stress. This nonlinear tensorial operator is significant in that it allows both the flow and evolutionary laws to be fully associative (and therefore easily integrated), which greatly influences the multiaxial response under non-proportional load paths, and in the case of nonisothermal histories, introduces an instantaneous thermal softening mechanism proportional to the rate of change in temperature. In addition to this nonlinear compliance operator, a new, consistent, potential preserving, internal strain unloading criterion has been introduced to prevent abnormalities in the predicted stress-strain curves during unloading and reversed loading of the external variables. These features make **GVIPS** accurate in relaxation as well as able to handle any nonproportional loading present within the composite.

The **GVIPS** flow and evolution equations are, respectively,

---

[1] TIMETAL 21S is a registered trademark of TIMET, Titanium Metals Corporation, Toronto, OH.

$$\dot{\varepsilon}^i_{ij} = \begin{cases} 0 & \text{if } \hat{F} < 0 \\ \dfrac{3\left\|\dot{\varepsilon}^i_{ij}\right\|\Sigma_{ij}}{2\sqrt{J_2'}} & \text{if } \hat{F} \ge 0 \end{cases}$$

$$\dot{A}_{ij} = \begin{cases} Q_{ijmn} E_{mnkl} b_{kl} & \text{if } a_{ij}\Sigma_{ij} < 0 \\ b_{ij} & \text{if } a_{ij}\Sigma_{ij} \ge 0 \end{cases}$$

$$\dot{a}_{ij} = L_{ijkl}\left(\dot{A}_{kl} - \theta_{kl}\dot{T}\right), \tag{5}$$

where the dot represents time differentiation, A_{ij} is the deviatoric back strain tensor, a_{ij} the deviatoric back stress tensor, T is temperature, and

$$\left\|\dot{\varepsilon}^i_{ij}\right\| = \sqrt{\frac{2}{3}\dot{\varepsilon}^i_{ij}\dot{\varepsilon}^i_{ij}} = \frac{\mu_o \hat{F}^n}{\kappa} \quad \text{(equivalent inelastic strain rate)}$$

$$L_{ijkl} = Q^{-1}_{ijkl} = \frac{\kappa_o^2}{3B_0\left(1 + B_1 p G^{p-1}\right)}\left(\delta_{ik}\delta_{jl} - \frac{3B_1(p-1)G^{p-2}a_{ij}a_{kl}}{\kappa_o^2\left[1 + B_1 p G^{p-1}(2p-1)\right]}\right) \quad \text{(stiffness operator)}$$

$$b_{ij} = \dot{\varepsilon}^i_{ij} - \left(\frac{3\beta\kappa\dot{\bar{\varepsilon}}^{vp} H_v[Y]}{2\kappa_o^2\sqrt{G}} + \frac{3R_\alpha B_0 G^q}{\kappa_o^2}\right) a_{ij}$$

$$\theta_{ij} = \frac{\partial B_0}{\partial T}\left(1 + B_1 p G^{p-1}\right)\frac{3a_{ij}}{\kappa_o^2} \quad \text{(dynamic thermal recovery operator)}$$

$$\hat{F} = \left\langle \frac{\sqrt{J_2'}}{\kappa} - Y \right\rangle \quad \text{(threshold function)}$$

$$Y = \left\langle 1 - \beta\sqrt{\hat{G}} \right\rangle \quad \text{(yield stress function)}$$

$$\hat{G} = \frac{I_2'}{\kappa_o^2} \quad \text{(back stress function)}$$

$$I_2' = \frac{3}{2}a_{ij}a_{ij}, \quad J_2' = \frac{3}{2}\Sigma_{ij}\Sigma_{ij} \quad \text{(stress invariants)} \tag{6}$$

and E_{ijkl} are elastic stiffness coefficients, $H_v[\bullet]$ is the Heaviside unit step function, and <•> are Macauley brackets. Note that the $(2p-1)$ term in the denominator of the stiffness operator L_{ijkl} differs from the erroneous $(6p-5)$ term reported earlier by Arnold et al (1996a,b). This minor mistake has been found to influence only the tensile response (dealt with previously) slightly as only the shear components are affected and can be corrected for by a slight modification to B_1 in Table 3. The temperature-independent material parameters are: κ_o, n, B_1, p, and q, while the temperature-dependent material parameters are: κ, μ_o, B_0, R_α, and β. Interpolation functions defined by Arnold et al (1996a) are employed to determine the material parameters for TIMETAL 21S at temperatures other than the reference temperature of 650 °C. A limitation of the material characterization is that above 704 °C, material parameters are taken to be those at 704 °C. Thermo-elastic and viscoplastic material parameters at various temperatures are presented in Table 3.

Temp (°C)	E (GPa)	α (1×10^{-6}/°C)	κ (MPa)	μ (MPa/sec)	B_0 (MPa)	R_α (1/sec)	β
23	114.1	7.717	1029	667.6	6.908×10^{-5}	0	0.001
300	107.9	9.209	768.4	137.8	1.035×10^{-4}	0	0
500	95.1	10.70	254.2	1.45×10^{-3}	2.756×10^{-4}	1.68×10^{-7}	0
650	80.7	12.13	5.861	6.19×10^{-9}	5.870×10^{-4}	1.00×10^{-6}	0
704	59.7	14.09	0.756	1.13×10^{-11}	6.346×10^{-4}	6.01×10^{-5}	0
temperature-independent: $\nu = 0.365$, $n = 3.3$, $B_1 = 0.0235$, $p = 1.8$, $q = 1.35$							

Table 3. TIMETAL 21S material properties.

4. Debonding/Failure Models

4.1 Curtin Effective Fiber Breakage Model

As mentioned previously, prior researchers have employed the Curtin effective fiber breakage model (Curtin, 1991, 1993) to simulate the longitudinal tensile behavior of metal matrix composites (MMCs) (Walls et al, 1991). This model has been incorporated into **MAC/GMC**, and later predictions for the longitudinal failure behavior of SiC/Ti composites made using the Curtin model will be presented. It is important to note that, while this model has been applied to MMCs in the past, it was originally developed for application to PMCs and ceramic matrix composites (CMCs). The Curtin model simulates all fibers in a composite as one effective fiber whose effective elastic modulus, E_f^*, is progressively decreased according to the equation,

$$E_f^* = \frac{1}{2}\left\{1 + \exp\left[-\frac{D}{2\tau_0\, L_0 \sigma_0^m}\left(E_f\, \varepsilon_{mech}^f\right)^{m+1}\right]\right\} E_f\,. \tag{7}$$

In this equation, E_f is the original elastic modulus of the fiber, D is the fiber diameter, τ_0 is the critical shear stress for fiber-matrix interfacial sliding, L_0, σ_0, and m are the characteristic length, characteristic strength, and Weibull modulus from the fiber strength distribution, and ε_{mech}^f is the longitudinal mechanical strain in the fiber. Equation (7) is developed based on the Weibull statistical strength characteristics of the fiber, along with sliding interface and shear transfer arguments (Curtin, 1991).

The Curtin model also provides a methodology for predicting longitudinal composite failure; it is taken as the composite stress at which the longitudinal stress in the effective fiber reaches a maximum. This maximum fiber stress occurs at a critical fiber mechanical strain of,

$$\left(\varepsilon^f_{\text{mech}}\right)^* = \frac{1}{E_f}\left[\frac{2\tau_0 L_0 \sigma_0^m}{D}x\right]^{\frac{1}{1+m}}, \tag{8}$$

where *x* is the smallest positive value that satisfies the equation,

$$1+\left[1-(m+1)x\right]\exp(-x)=0\,. \tag{9}$$

One difficulty associated with the Curtin effective fiber breakage model is that the parameter τ_0 is not well known. Fiber push-out tests on SiC/Ti have indicated that it lies in the range 30 – 50 MPa (Walls et al, 1991). Herein, a value of 48 MPa was employed for τ_0, which agrees with the value used by Walls et al (1991) in their investigation of SiC/Ti. The remaining Curtin model parameters employed for the SCS-6 fiber are: $D=142$ μm; $L_0=25.4$ mm; $\sigma_0=4200$ MPa; $m=10$. For these parameters, the Curtin model yields a value of $x=0.2022$ and $\left(\varepsilon^f_{\text{mech}}\right)^*=0.0111$ MPa from eqns (8) and (9). Using these values, it is possible to plot the uniaxial Curtin model effective fiber constitutive response by assuming that the average fiber stress is given by,

$$\sigma^f_{\text{avg}} = E^*_f\,\varepsilon^f_{\text{mech}}\,. \tag{10}$$

For the Curtin model parameters given above, such a plot is provided in Fig. 3. It is clear from this figure that the effective fiber stress does indeed reach a local maximum which may be used as a criterion for composite failure.

*4.2 Evolving Compliant Interface (**ECI**) Model*

In **MAC/GMC** version 2.0 (Wilt and Arnold, 1996) an imperfect bonding model based on the Achenbach and Zhu (1989) concept of a flexible interface was developed, incorporated, and utilized (Goldberg and Arnold, 1999). For the present investigation this modified concept has been further extended and applied to model discrete longitudinal fiber breakage in composite materials. The flexible interface model was originally included in **GMC** by Aboudi (1988), then included in **MAC/GMC** by Wilt and Arnold (1996), and later included in the reformulated version of **GMC** by Bednarcyk and Pindera (2000). The original Achenbach and Zhu (1989) method is based on allowing discontinuities in the displacement components that are normal or tangential to a given subcell interface. The discontinuity, or jump, in the displacement component is related to the appropriate stress at the interface by a debonding parameter, R_n or R_t. That is,

$$\left[u_n\right]^I = R_n\,\sigma_n\big|^I \qquad\qquad \left[u_t\right]^I = R_t\,\sigma_t\big|^I\,. \tag{11}$$

Here, *I* refers to the interface in question, while *n* and *t* refer to the normal and tangential components, respectively. Initially, when this methodology was used in conjunction with **GMC**, the debonding parameters were treated as constant, and the imperfect bonding was present at all times. Thus, the compliance of the simulated interface could be chosen by selecting the values of the debonding parameters; a value of zero would correspond to perfect bonding, while a large value would correspond to complete debonding. This form of the debonding model will henceforth be referred to as the **constant compliant interface** (**CCI**) model.

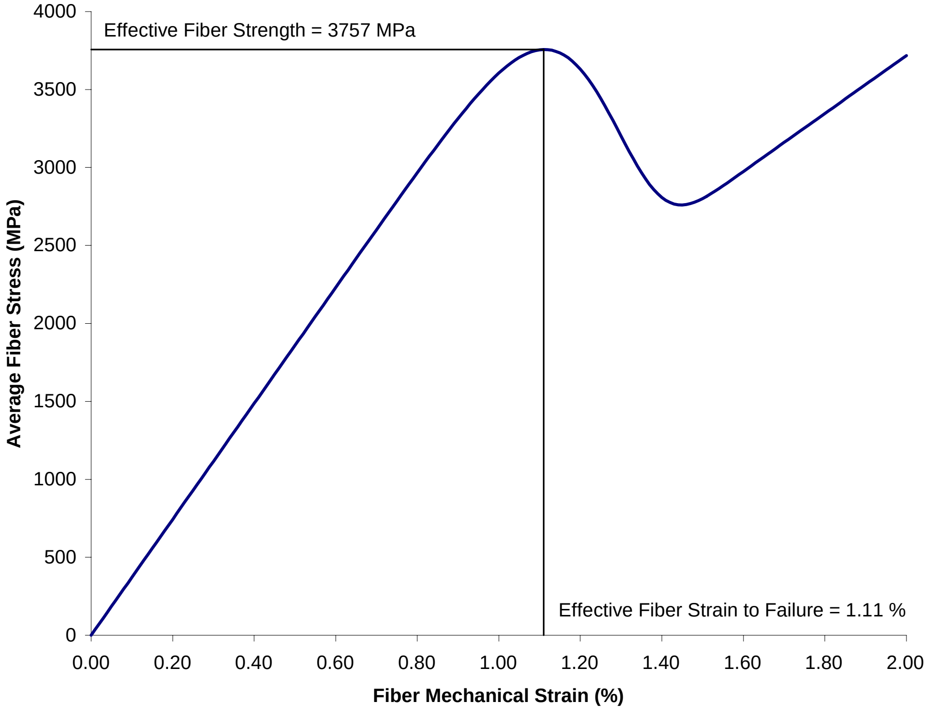

Fig. 3. Curtin model uniaxial effective SCS-6 fiber constitutive behavior.

When Wilt and Arnold (1996) first incorporated the **CCI** model into **MAC/GMC**, two distinctions from others' work arose. First, interfaces were given a debond strength. Thus, at stresses below the debond strength, the interface would remain perfectly bonded. Then, once the interfacial stress exceeded the interfacial debond strength, the interface would become flexible for all remaining time. Second, since **MAC/GMC** employs a rate (tangent) formulation of **GMC**[2], the flexible interface model was employed in rate form. Thus, for the **MAC/GMC** implementation, eqn (11) was replaced by,

$$\begin{array}{ll} \left[\dot{u}_n\right]^I = R_n\,\dot{\sigma}_n\big|^I; & \sigma_n\big|^I \geq \sigma_{DB}\big|^I \\ & \qquad\qquad , \\ \left[\dot{u}_t\right]^I = R_t\,\dot{\sigma}_t\big|^I; & \sigma_t\big|^I \geq \sigma_{DB}\big|^I \end{array} \tag{12}$$

where dotted terms are rates (time derivatives), and $\sigma_{DB}\big|^I$ is the debond strength of interface *I*. Typically, when using the **CCI** model within **MAC/GMC**, one would select large values for the debonding parameters thus simulating complete debonding at the interface once the interfacial debond strength had been exceeded. As a result of this procedure, the interfacial stress becomes constant (with the value of the debond strength) once debonding occurs. It would also be possible to allow the interface to become flexible, but not completely debonded, by selecting a moderate value for the appropriate debonding parameter. This previous **MAC/GMC** implementation, however, did not permit the interfacial stress to decrease after debonding while the global stress applied to the composite continued to increase. Obviously, this type of local unloading is desirable as it is a more accurate representation of the physics of local debonding or breakage within an actual material.

---

[2] **GMC** is used to determine local and global stress and strain rates, which are then integrated outside of the model to determine the local and global stresses and strains.

For the present investigation, a new local debonding/failure model that allows local unloading of stresses even as global loading continues was developed and incorporated into **MAC/GMC**. The new model is still based on the concept of a flexible interface, however, by allowing the debonding parameters to evolve with time, the desired local unloading may occur naturally. This implementation of the flexible interface model will be referred to as the **evolving compliant interface** (**ECI**) model. In the **ECI** model, eqn (12) is replaced by,

$$\begin{array}{ll} \left[\dot{u}_n\right]^I = R_n(t)\,\dot{\sigma}_n\big|^I + \dot{R}_n(t)\,\sigma_n\big|^I & \sigma_n\big|^I \geq \sigma_{DB}\big|^I \\ \left[\dot{u}_t\right]^I = R_t(t)\,\dot{\sigma}_t\big|^I + \dot{R}_t(t)\,\sigma_t\big|^I & \sigma_t\big|^I \geq \sigma_{DB}\big|^I \end{array} , \tag{13}$$

where the time dependence of the normal and tangential debonding parameters, R_n and R_t, respectively, are taken to have the following form;

$$R(t) = \Lambda\left[\exp\left(\hat{t}/\mathrm{B}\right) - 1\right]. \tag{14}$$

Here, Λ and B are empirical constants specific to the interface, and $\hat{t}$ is the time since debonding. Note that while Λ affects only the magnitude of the expression for $R(t)$, changes in the parameter B affect the character of the exponential functionality in eqn (14). Calculating the sensitivity of the debonding parameter ($R(t)$) to the material constants (Λ and B), that is;

$$S_\Lambda = \frac{d\,R(t)}{d\,\Lambda} = \exp\left(\hat{t}/\mathrm{B}\right) - 1 \tag{15}$$

$$S_\mathrm{B} = \frac{d\,R(t)}{d\,\mathrm{B}} = -\hat{t}\,\frac{\Lambda}{\mathrm{B}^2}\exp\left(\hat{t}/\mathrm{B}\right) \tag{16}$$

we see immediately that the sensitivities have opposite signs. Thus an increase in Λ causes an increase in $R(t)$ (at a given time), while an increase in B causes a decrease in $R(t)$ (at a given time). This is a beneficial feature of the form of eqn (14) as the parameters compete and can thus be used to compensate for changes in one another. Furthermore, S_B is dependent on both B and Λ while S_Λ is independent of Λ.

Fig. 4 and Fig. 5 illustrate the effects of changing Λ and B on the debonding parameter ($R(t)$) as a function of time. These figures show that, once debonding has occurred, the debonding parameter (and hence the interfacial compliance) increases exponentially with time. Comparing Fig. 4 and Fig. 5, it is clear that the debonding parameter, $R(t)$, is significantly more sensitive to changes in B (see eqn (16)) than to changes in Λ (see eqn (15)). For example, changing B by a factor of two in Fig. 5 has a much greater effect on the debonding parameter evolution than does changing Λ by a factor of two in Fig. 4.

At first glance it may seem more natural to allow the debonding parameter to be a function of a local variable, such as stress at the interface, rather than time. However, this actually disallows local unloading because the debonding parameter and the local stress each tend to converge. In this condition, the interfacial compliance reaches a value that is sufficiently high to prevent accumulation of additional local stress, which then prevents the debonding parameter from growing larger. Once the debonding parameter stops growing larger, it is a constant, and the effect of debonding becomes equivalent to that of the **CCI** model, as represented by eqn (12). Obviously, local unloading then cannot occur.

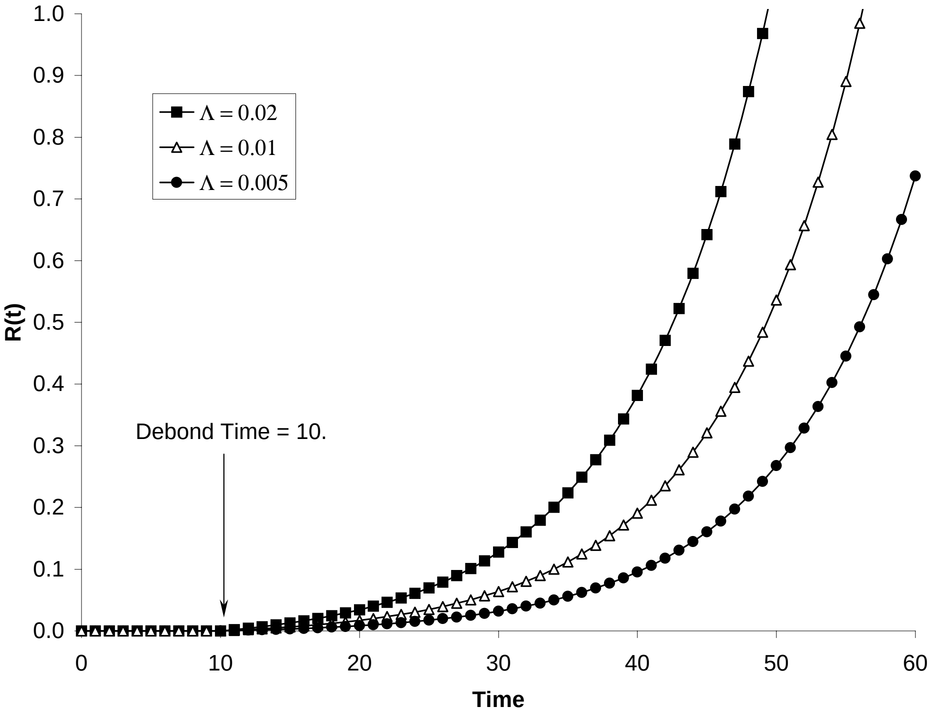

Fig. 4. Debonding parameter functional dependence on Λ for $B = 10$.

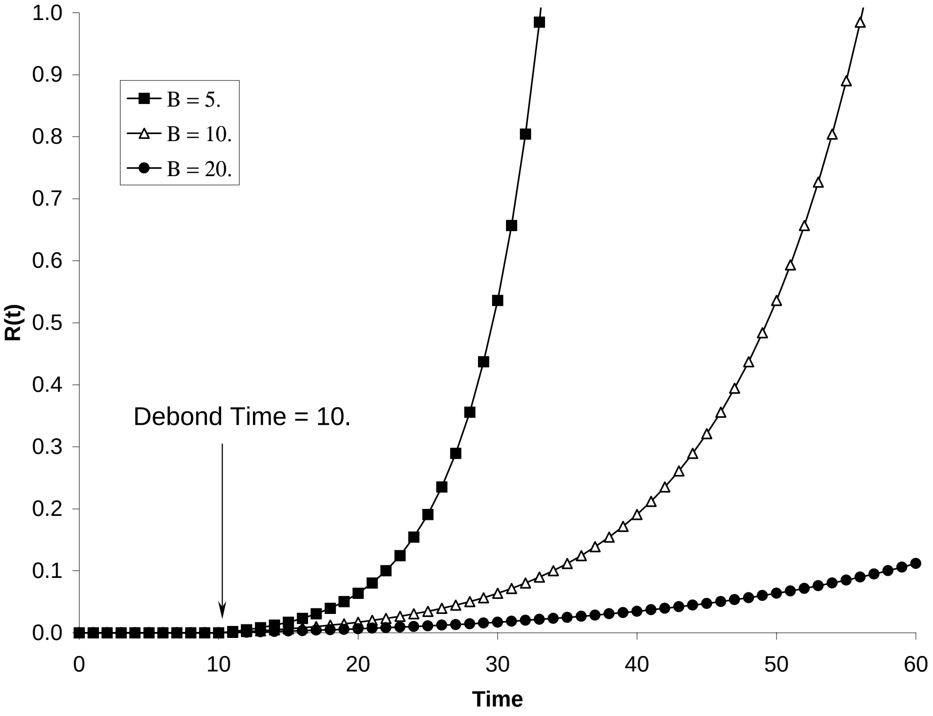

Fig. 5. Debonding parameter functional dependence on B for $\Lambda = 0.01$.

The exponential form for the debonding parameters (eqn (14)) was chosen because it allows the local stress to unload smoothly, and the parameters Λ and B can be chosen to provide a realistic global response. Other functional forms were examined. A linear form, for instance, did not allow the debonding parameters to evolve sufficiently quickly so as to allow the local stress to unload unless the slope of the linear function was quite high. However, this high slope then caused difficulties due to the rapid initial growth of the debonding parameters. Of the many functional forms that were examined for *R(t)*, the exponential form provided the best combination of features.

5. Model Application and Characterization

Fig. 6 illustrates how the **ECI** model is applied to simulate fiber breakage in a unidirectional composite. The figure shows a **GMC-TP** repeating unit cell consisting of eight subcells employed to represent a unidirectional composite. Here, a weak interface surface is placed within the fiber constituent, with its outward normal parallel to the fiber (and loading direction). The strength, σ_{DB}, of the interface may now be associated with the ultimate longitudinal tensile strength of the fiber, such that when the fiber stress reaches this value, the interface will debond and the longitudinal stress in the fiber will unload. A natural consequence of employing the simple unit cell shown in Fig. 6 is that once the longitudinal fiber stress exceeds σ_{DB}, breakage of all fibers within the composite is simulated, as in this case the unit cell represents the periodic geometry of an actual composite and thus repeats infinitely in all three Cartesian directions. The simulated longitudinal tensile behavior of a 25% SCS-6/TIMETAL 21S composite (at 650 °C) represented by the repeating unit cell shown in Fig. 6 is shown in Fig. 7. This figure includes the simulated local stress in the fiber (plotted versus the applied global strain), as well as the simulated global stress-strain response of the composite. In this case, the following debond parameters (chosen for illustrative purposes) were employed: $\sigma_{DB} = 3984$ MPa; $B = 10$ s; and $\Lambda = 1.45 \times 10^{-6}$ MPa^{-1}. Clearly, when the single fiber in the unit cell representation fails at 3984 MPa, simultaneous failure of all fibers in the composite is simulated, and, as the stress in the fiber(s) unload(s), the global composite stress decreases as well. Since the global composite stress reaches a maximum (of 1195 MPa) after which the stress-strain curve attains a physically unrealistic negative slope, this stress may be used as a simulated ultimate tensile strength (UTS) for the composite.

Also indicated on Fig. 7 are two of the stages identified in the characteristic longitudinal behavior of SiC/Ti composites by Brindley and Draper (1993). In stage I, both the fiber and matrix deform elastically, while in stage II, the matrix has yielded. Since the repeating unit cell contains only one fiber, stage III, which in reality involves failure of the weaker fibers, is not present. Once the single fiber fails, the global stress supported by the composite begins to decrease, which is clearly not realistic.

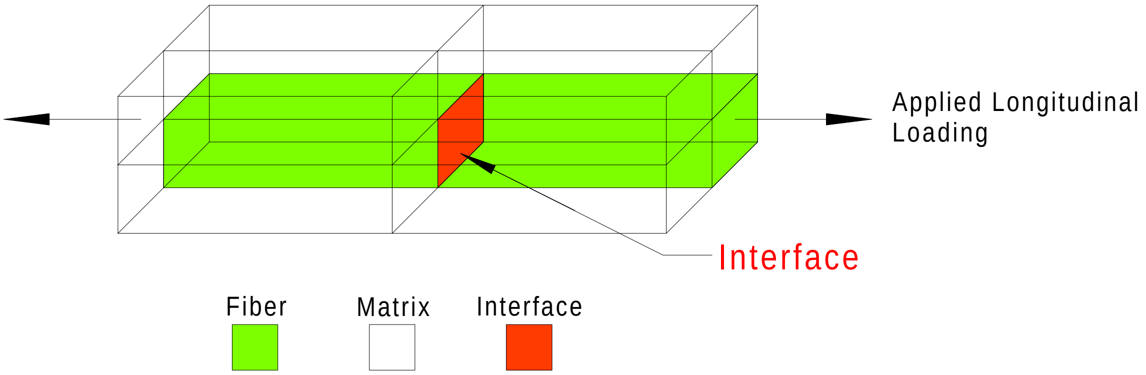

Fig. 6. Simple example of the application of the new debonding model to the longitudinal failure of unidirectional composites. A weak internal interface is placed within the fiber – interfacial failure then simulates failure of the fiber.

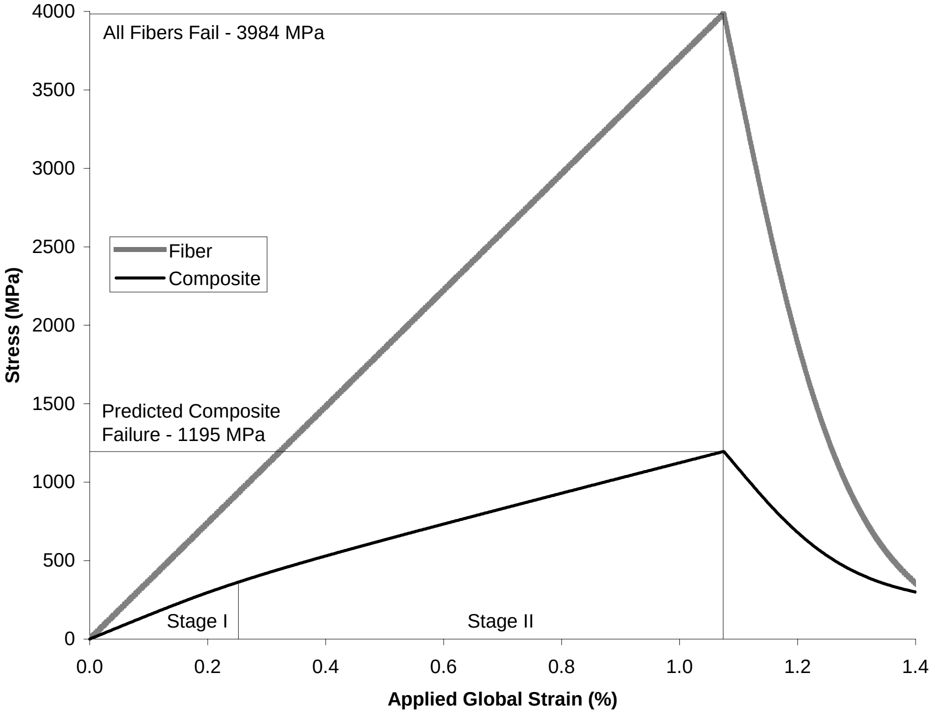

Fig. 7. Simulated longitudinal tensile response of a 25% SCS-6/TIMETAL 21S composite at 650 °C represented by the unit cell shown in Fig. 6.

If a more complex unit cell, like that shown in Fig. 8, is employed, a much more realistic approximation of the actual composite deformation and failure can be obtained. Note that execution of **MAC/GMC** using a unit cell with such a large number of subcells has become computationally reasonable due to the availability of the reformulation of the **GMC** equations. The unit cell shown in Fig. 8 contains 28 individual fibers, each of which may be given a different strength. A natural source for these fiber strengths is a vendor-supplied fiber strength histogram, like that shown in Fig. 9 for the SCS-6 silicon carbide fiber. As the figure indicates, the actual distribution of fiber strengths can be simulated by the 28 fibers present in the repeating unit cell. The unit cell still repeats infinitely, so a longitudinal tensile simulation will still not truly represent discrete longitudinal fiber breakage (rather, the breakage of each fiber will represent the breakage of one twenty-eighth of all the fibers in the simulated composite), but clearly the approximation is significantly more realistic.

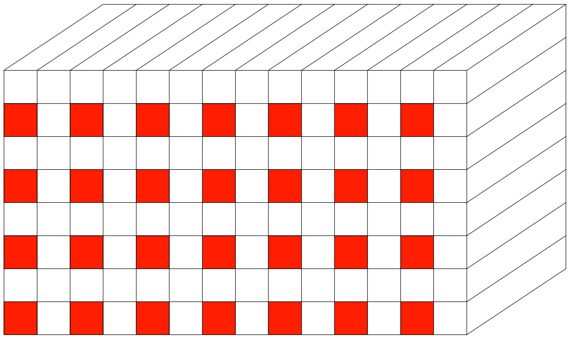

Fig. 8. Actual **GMC-TP** repeating unit cell employed for modeling the longitudinal failure of unidirectional composites.

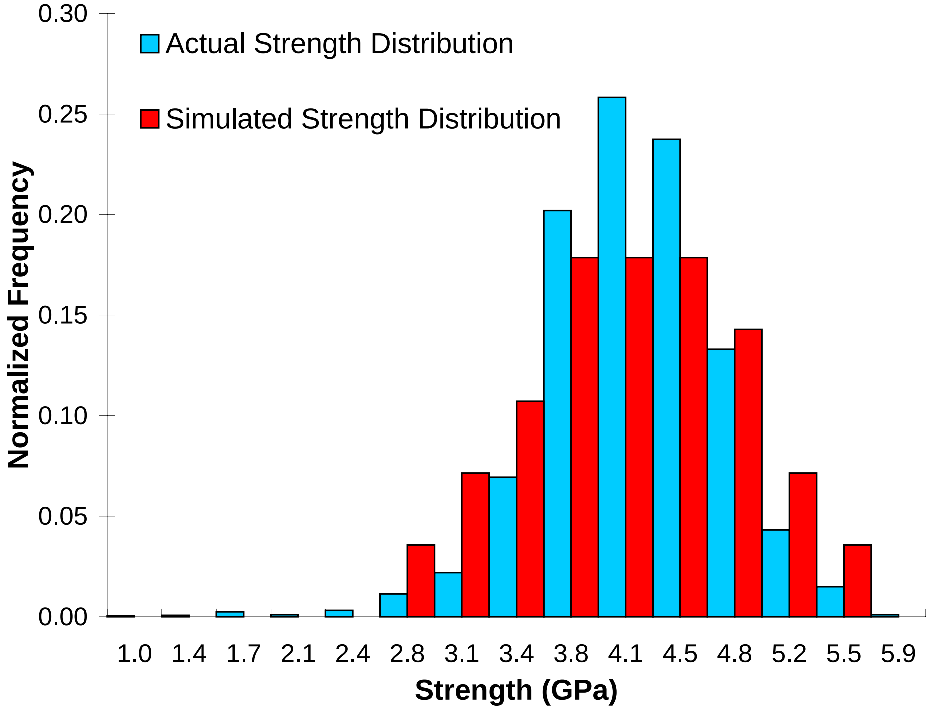

Fig. 9. Actual and simulated fiber strength distribution for SCS-6 SiC fibers.

The simulated longitudinal tensile behavior of a 25% SCS-6/TIMETAL 21S composite (at 650 °C) represented by the repeating unit cell shown in Fig. 8 is shown in Fig. 10. Here, the σ_{DB} of each of the 28 fibers in the repeating unit cell were taken from the simulated distribution shown in Fig. 9 (but modified based on fiber strength temperature dependence data, Mall et al, 1998), while values for Λ and B identical to those used to generate Fig. 7 were employed. Now, rather than all fibers failing at once, fibers modeled using a lower strength begin to fail first, and the experimentally observed stage III of the deformation behavior is now able to be simulated even when **GMC**'s periodic boundary conditions are employed. As the failed fibers unload the stress they were carrying, and as they cease to contribute to the composite stiffness, the slope of the predicted stress-strain curve begins to decrease. Once eight fibers have failed (representing over one quarter of all fibers), the global composite stress begins to decrease (as the strain applied to the composite continues to increase), indicating simulated global failure for the composite. The difference in the predicted strength for the composite between the single fiber representation and the 28 fiber representation is striking: 1195 MPa versus 967 MPa – a difference of 24%. As will be shown, use of the 28 fiber representation allows favorable comparison with experiment.

It should be noted that the **ECI** model accounts for the aggregation of complex effects associated with local fiber failures using a simplified mechanism. In an actual composite, when a fiber fractures, the stress is released and unloaded only in a local region near the fracture. Due to shear stress along the fiber matrix interface, local debonding may occur, and the longitudinal stress in the fiber increases as the distance from the fracture increases. In fact, a single fiber may fracture many times, each time decreasing the average stress in the fiber, before final failure of the composite occurs (Reifsnider and Highsmith, 1982). These local fractures are thus decreasing the effective fiber volume fraction of the composite, although no single fiber is immediately rendered completely ineffective. Since **GMC** has an inherent lack in the coupling of shear and normal stresses, the aforementioned interfacial shear stress does not arise in simulated normal tensile tests. Thus, in applying and characterizing the **ECI** model (as implemented in **MAC/GMC**) we are attempting to overcome this lack of shear coupling while obtaining the same global

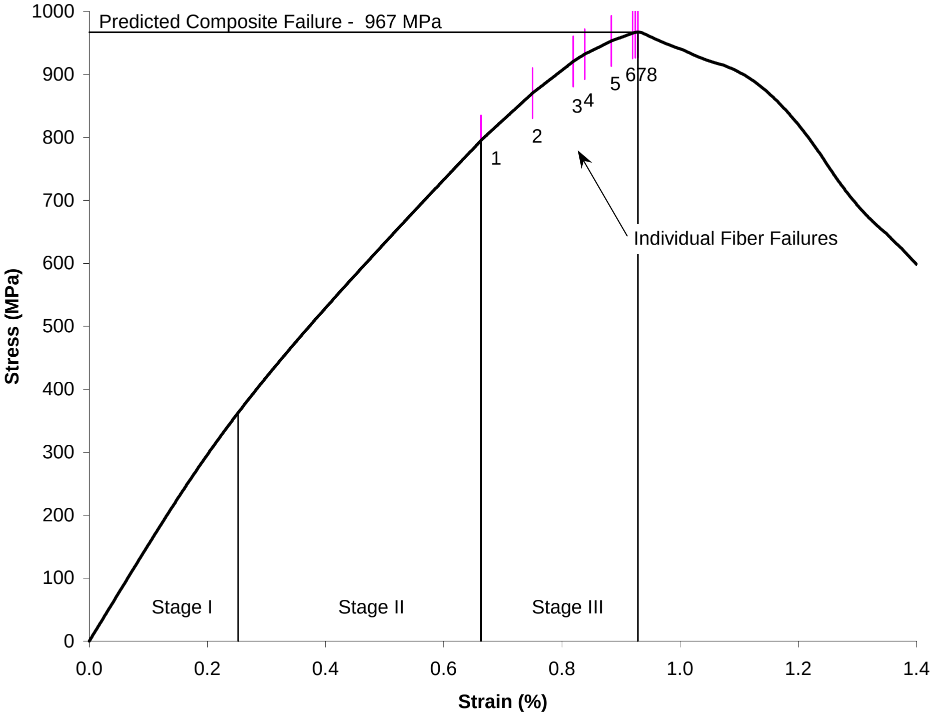

Fig. 10. Simulated longitudinal tensile response of a 25% SCS-6/TIMETAL 21S composite at 650 °C represented by the unit cell shown in Fig. 8.

response brought about through actual mechanisms of fragmentation, shear-lag stress transfer, and local debonding. The effects of the actual process of local fiber fragmentation, debonding, and transfer of shear to the matrix are simulated by unloading the longitudinal stress in one twenty-eighth of the fibers at a time. The simulated state after one such fiber has completely unloaded its stress corresponds to an actual composite in which a sufficient number of local fractures have occurred so as to lower the effective fiber volume fraction by one twenty-eighth.

As mentioned previously, global longitudinal failure of the composite will be taken as the point at which the simulated global stress-strain curve attains a negative slope. Although this failure criterion agrees with the spirit of the Curtin model failure criterion (composite failure when the effective fiber stress-strain curve attains a negative slope, Fig. 3), it is, in actuality, employed for the sake of convenience rather than for any true physicality with which it is associated. In a real composite, global failure occurs via matrix fracture that links fractured fiber regions. Clearly, the physics of this process are as complex as that associated with each individual fiber failure (discussed above). Modeling this process accurately, from a mechanistic sense, is beyond the scope of the **GMC** approach employed in this study. The maximum that is present in the simulated composite stress-strain curve (see Fig. 10) is brought about by the unloading of stress in the failed fibers. It is a unique feature of the approach employed herein, and it is convenient for use as a global failure criterion since it requires no additional correlation with experiment. Further, the region of the predicted stress-strain curve that follows the maximum is clearly unrealistic in that an actual composite fails abruptly in longitudinal tension. As will be shown, since our failure criterion requires the predicted stress-strain curve to attain a slope of zero (which corresponds to zero effective stiffness), the model tends to overpredict the stiffness decrease in the composite prior to failure.

In using this approach, which attempts to capture the global effects of the influence of local fiber fragmentation, debonding, and transfer of shear to the matrix, as well as the final fracture of the composite, but does not explicitly model the effects in a mechanistic sense, one can expect limitations of the applicability of the approach. However, as will be shown, the **ECI** model as implemented in **MAC/GMC** can be quite useful (and accurate) for modeling the longitudinal failure behavior of composites. Further, the probablistic nature of the fiber strength has been incorporated through the use of the fiber strength histogram.

In order to allow the **ECI** model to be as accurate as possible considering its approximate mechanistic nature, several factors must be considered. The debonding parameters, Λ and B, provide the model with the flexibility to model many different scenarios. However, it is desirable to link these parameters in some way to physical quantities associated with the composite being analyzed. That is, we seek to choose baseline values for Λ and B based on correlation with experimental data, and then to relate the parameter values for other simulated conditions to these baseline values. As will be discussed below, the varying simulated conditions include the cross-section of the composite that is associated with a particular failure event (which is related to fiber volume fraction), the global strain rate, and the temperature.

5.1 Failure Event Cross-Section Effect

Fig. 11 shows the simulated longitudinal tensile response of the same 25% volume fraction SCS-6/TIMETAL 21S composite at 650 °C modeled previously where a unit cell with an increasing number of fibers was employed. The stress-strain curve labeled “1 Fiber” was plotted previously in Fig. 7, while the stress-strain curve labeled “28 Fibers” was plotted previously in Fig. 10. In all cases the debond parameters, $\mathrm{B} = 10\,\mathrm{s}$ and $\Lambda = 1.45 \times 10^{-6}$ MPa^{-1}, were used, and the σ_{DB} values for each case were chosen to provide a good representation of the actual fiber strength histogram shown in Fig. 9 (with a strength reduction due to elevated temperature), given the number of fibers in the unit cell representation.

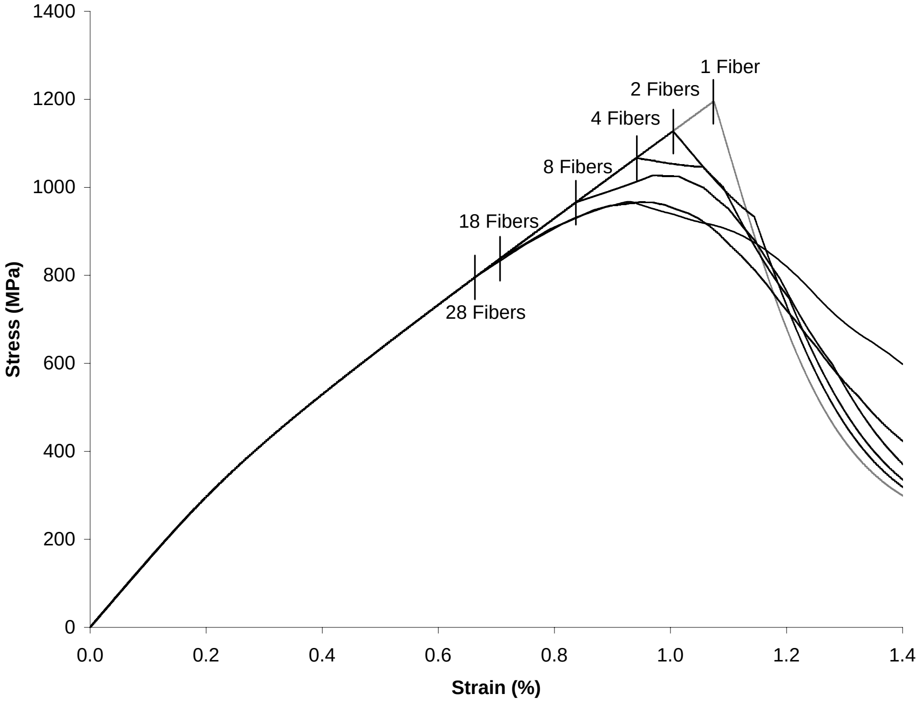

Fig. 11. Simulated longitudinal tensile response of a 25% SCS-6/TIMETAL 21S composite at 650 °C represented by unit cells with the indicated number of fibers. Short vertical lines show the location of the first fiber failure for the indicated unit cell representation.

Fig. 11 shows that, as the number of fibers in the unit cell decreases, the effect of the first fiber failure on the global response of the composite increases. In all cases, the first fiber failure event (indicated by the vertical line in Fig. 11) decreases the slope of the simulated stress-strain curve, but for the 1, 2, and 4 fiber unit cell representations, this slope immediately becomes negative following the first fiber failure. For the 8, 18, and 28 fiber unit cell representations, the slope of the simulated stress-strain curve remains positive until more fibers have failed. This characteristic of the **ECI** model is related to the ratio of the composite cross-sectional area that fails as part of a single event, relative to the remaining cross-section left intact after this failure event. When the fiber in the single fiber representation (see Fig. 6) of the 25% volume fraction composite fails, a full 25% of the unit cell cross-section is affected and begins to unload its stress. This leaves only 75% of the composite intact to accept the unloaded stress and support the stress from the additional global loading (which continues to increase). Furthermore, the intact portion of the composite consists entirely of matrix material, which is significantly more compliant than the composite as a whole. The result is the steep negative initial post-failure slope of the curve associated with the single fiber unit cell representation. In contrast, when a greater number of fibers is included in the unit cell representation (see Fig. 8), each fiber failure event affects only a small fraction of the composite cross-section. In the case of the 28 fiber representation, the first fiber failure affects only 0.89% of the cross-section, leaving 99.11% of the composite intact to accept the unloaded stress and to support the additional stress from continued global loading. The result is that the first fiber failure has only a small effect on the simulated stress-strain response. Seven additional fibers must fail (see Fig. 10) before the slope of the predicted stress-strain curve becomes negative, which indicates global failure.

From the above discussion it follows that utilization of the same **ECI** model parameters, Λ and B, for different composite volume fractions is not warranted, even for unit cell representations with the same number of fibers. As discussed in Section 4.2, these parameters control the initial unloading characteristics of the fibers, which in turn affect the simulated composite response. As discussed above, the simulated composite response is also affected by the fraction of the composite cross-section associated with each failure event. However, this effect is actually an undesirable artifact of our method for modeling the process of local fiber fragmentation, debonding, and shear-lag stress transfer. In reality, the mechanisms responsible for this complex process, and the effect of the process on the composite response, are not directly influenced by the fiber volume fraction. The local process is the same whether the composite is 20% fibers or 50% fibers. This is not to say that the overall response of such different composites is the same, only that the micro-mechanisms associated with fiber breakage are the same in both composites. As discussed above, for a specific composite this artifact can be eliminated by using a sufficiently large number of fibers in the composite unit cell representation (see Fig. 11). In order to eliminate this artifact for more general composites (i.e., those with different fiber volume fractions) and allow each simulated failure event to have a consistent initial effect on the composite response, the **ECI** model parameters will be linked to the percentage of the composite cross-section associated with a particular failure event.

To establish this linkage, the results shown in Fig. 12 were used. The baseline case plotted in Fig. 12 is a detail of a longitudinal stress-strain curve for 25% SCS-6/TIMETAL 21S in which 4% of the fiber cross-section, which corresponds to 1% of the composite cross-section (X), is permitted to fail. We then double the failure cross-section to 2% and seek an **ECI** model parameter B that results in consistent initial composite post-failure behavior. Note that a constant value of $\Lambda = 1.45 \times 10^{-4}$ MPa^{-1} was employed. As Fig. 12 indicates, doubling the failure cross-section to 2% while leaving B (= 10 s) unchanged, results in a composite stress-strain curve that is too steep compared to the baseline case. Conversely, employing a value of $B = 40$ s, which is four times that of the baseline case, results in a curve that is not steep enough. If the baseline value of B is doubled to 20 s however, the X = 2% composite initial post-failure behavior is consistent with the baseline case. Thus it appears that in order to adjust the **ECI** model parameters to remain consistent across cases with different failure cross-sections, it is possible to simply adjust the parameter B by the percentage that the debonding cross-section has changed. Fig. 12 shows that this is indeed valid as a stress-strain curve is plotted for X = 0.5%, one-half

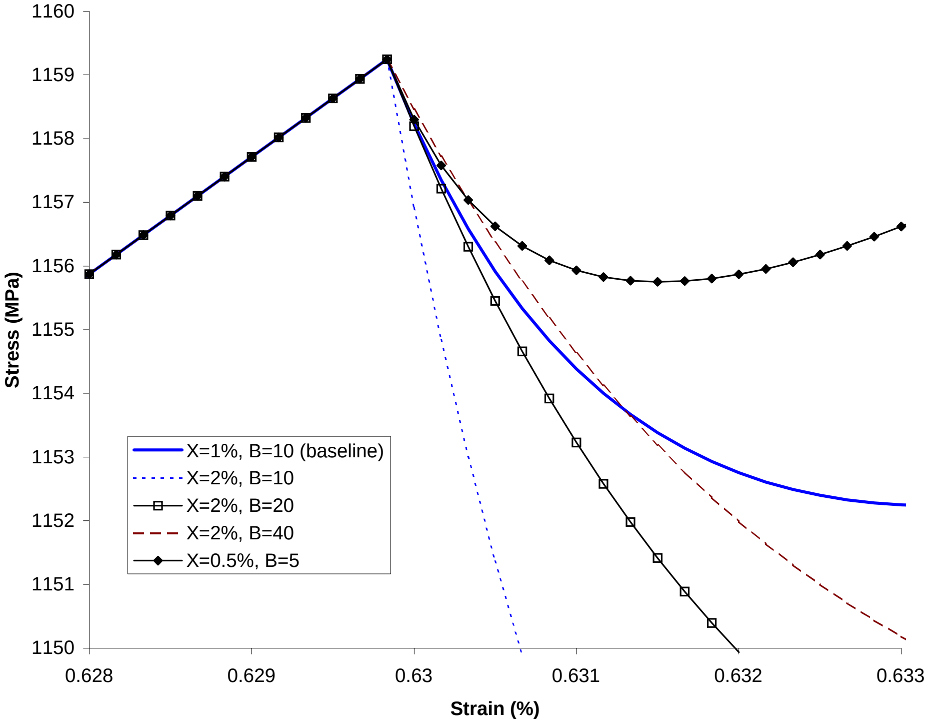

Fig. 12. Detail of simulated longitudinal stress-strain curves for 25% SCS-6/TIMETAL 21S used to characterize the failure event cross-section dependence of the debonding parameters. The percentage of the composite cross-section affected by the failure event (X) and the debonding parameter (B) are varied.

that of the baseline case. Employing a value of $\mathrm{B} = 5$ s, which is one-half that of the baseline case, once again provides consistent initial post-failure behavior. Note that we are concerned with the consistency of only the initial post-failure slope of the composite stress-strain curve, not the consistency of the composite stress-strain curve after complete unloading of a particular failed fiber. Clearly, as loading continues, the stress-strain curves of composites with different debonded cross-sections must diverge since they represent composites that now have different effective fiber volume fractions. Unlike the cross-section induced differences in the initial post-failure slope, differences in the composite stress-strain curve after complete unloading of a fiber has occurred are realistic. Clearly, the complete effective loss of 1% of a composite's cross-section should have a larger impact on the response than the complete effective loss of 0.5% of the composite's cross-section. This larger impact is evident in Fig. 12.

A clear procedure has thus emerged for modeling the longitudinal response of composite materials using the **ECI** model. A **MAC/GMC** repeating unit cell is chosen with a sufficient number of fibers to represent the vendor-supplied fiber strength histogram. The fiber strengths are assigned based on the histogram (and any available temperature dependence data), and the Λ and B debonding parameters, which are the same for all fibers, are chosen in order to achieve acceptable correlation with an experimental stress-strain curve for the material. This chosen value of B as well as the fiber volume fraction for the case become reference values, $\mathrm{B}_{\mathrm{ref}}$ and V_f^{ref}. Then, if the fiber volume fraction of the simulated composite changes, the parameter B can be changed by the identical percentage in order to allow each failure event to have an initial effect that is consistent with the baseline (reference) case. That is, B is calculated from,

$$\mathrm{B} = \mathrm{B}_{\mathrm{ref}}\left(\frac{V_f}{V_f^{\mathrm{ref}}}\right), \tag{17}$$

while the identical value for Λ is employed. Note that attempts were made to account for the cross-sectional dependence by altering Λ. However, utilization of B proved more effective as the debonding parameter $R(t)$ is more sensitive to its changes (see eqn (16) and Fig. 5).

5.2 Strain Rate Effect

An additional effect to which the debonding parameters should be linked is the global strain rate experienced by the composite. Since the debonding model is based on explicit time dependence (see eqn (14)), it is obvious that a set of parameters that provides good correlation with experiment for one strain rate may not allow the local stress to unload sufficiently quickly if the strain rate is increased. Conversely, if the strain rate is decreased, the previous set of parameters may cause the unloading to occur too quickly. This effect is an undesirable artifact of the explicit time dependence. It is reasonably obvious that, since the time dependence in the debonding model is scaled by the parameter B (see eqn (14)), it is possible to once again alter B by the percentage change in the global strain rate from a baseline case. However, since increasing B slows the unloading rate (see Fig. 12), if the strain rate is doubled, the reference B value must be divided by two (in order to speed up the unloading). Thus it is possible to choose the debonding model parameters based on correlation with experiment at one strain rate and subsequently alter them for application to any other strain rate. Consequently, eqn (17) can now be altered to include the effect of strain rate as well,

$$\mathrm{B} = \mathrm{B}_{\mathrm{ref}}\left(\frac{V_f}{V_f^{\mathrm{ref}}}\right)\left(\frac{\dot{\varepsilon}_{\mathrm{ref}}}{\dot{\varepsilon}}\right), \tag{18}$$

where $\dot{\varepsilon}$ and $\dot{\varepsilon}_{\mathrm{ref}}$ are the global strain rates for the current and reference cases, respectively.

5.3 Temperature Effect

One effect for which the debonding model cannot be easily characterized is that of temperature. Unlike the failure event cross-section and strain rate effects, the temperature effect is not an artifact of the model’s approach. It is likely that the way in which fibers fail and unload their stress is affected by temperature. Some of this effect is accounted for by the temperature-dependent fiber and matrix properties that are included within **MAC/GMC**. Further, the debond stress associated with the fibers can be altered (based on available data) to account for the effect of temperature on fiber strength. However, the temperature dependence of the in-situ local fiber failure characteristics (e.g., fragmentation frequency, debond length, degree of shear-lag stress transfer) on the global composite response cannot be simply included. Doing so would likely entail choosing the debonding parameters based on correlation at several temperatures and interpolating to determine the parameters at a particular temperature. This is undesirable from the standpoint of the effort such correlation would require and because additional experimental stress-strain curves would be needed. Thus, any temperature dependence of the post-failure fiber unloading behavior will be neglected in this study. It is proposed that, in light of the approximate nature of **GMC** and the built-in temperature dependence of the material constitutive models, neglecting the aforementioned temperature dependence will not have a significant effect on the validity and usefulness of the **ECI** model.

6. Results and Discussion

6.1 Nominally 35% Volume Fraction SCS-6/TIMETAL 21S

6.1.1 Monotonic Response

Fig. 13 shows the simulated and experimental longitudinal tensile response of nominally 35% SCS-6/TIMETAL 21S at 650 °C and 23 °C. The 650 °C case was chosen as the baseline (reference case) from which the debonding parameters were characterized, since at 650 °C residual stresses are less significant than at lower temperatures. In **MAC/GMC**, residual stresses are modeled by simulating a globally stress-free cool down from an elevated temperature, typically taken to be the consolidation temperature or the heat treatment temperature, to room temperature prior to simulating the actual thermo-mechanical loading. Hence, the residual stress state predicted by **MAC/GMC** may not be perfectly accurate. The 650 °C tensile simulation is performed by simulating a stress-free heat up to 650 °C after the cool down, and then applying the simulated mechanical loading. Thus, during the heat up, most of the residual stresses are eliminated, and the predicted initial stress state for the 650 °C case is likely more accurate than that of the 23 °C case. It is then logical to use this more accurate prediction to characterize the debonding model parameters.

The 28 fiber unit cell representation (see Fig. 8) was employed for the **ECI** model simulations shown in Fig. 13, and the strengths of the 28 fibers were assigned based on the histogram shown in Fig. 9. In order to account for the temperature dependence of the fiber strength, the strengths of the 28 fibers were reduced by 5.3% for the 650 °C case (Mall et al, 1998). Since the average fiber volume fraction of individual test specimens can vary by a small amount (1 to 3 %) from the nominal value (Bowman, 1999), and since fiber volume fraction variations on this order do have a noticeable effect on longitudinal tensile predictions, it was necessary to determine an accurate fiber volume fraction for use in the

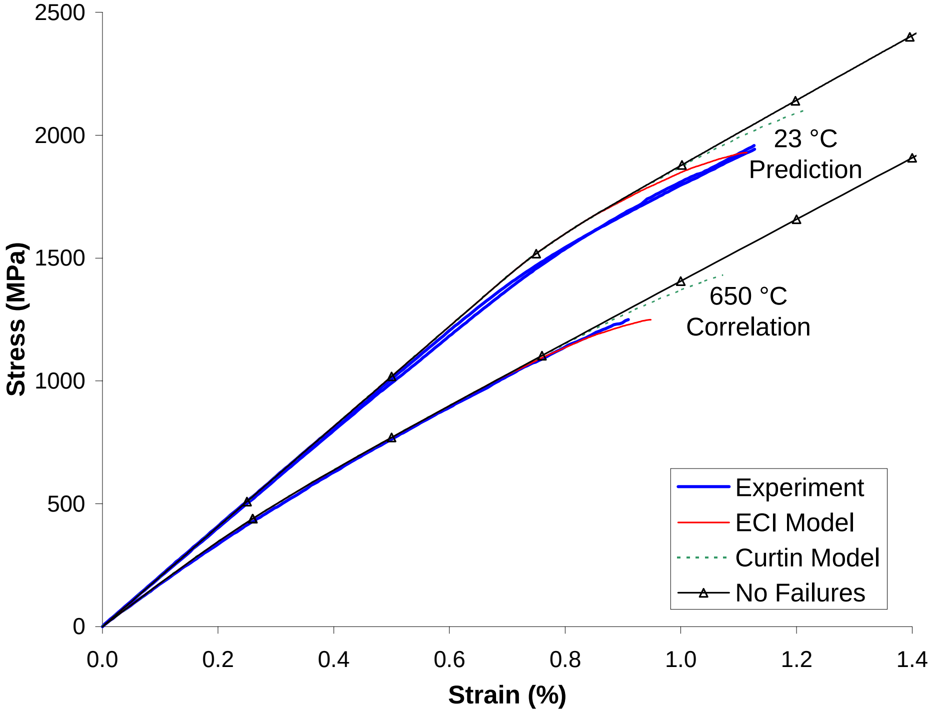

Fig. 13. Comparison of the simulated and experimental longitudinal tensile response of nominally 35% SCS-6/TIMETAL 21S. $\dot{\varepsilon} = 1.67 \times 10^{-4}$ s^{-1}.

simulations. This was done by varying the fiber volume fraction in a particular simulation (to the nearest 1%) until good correlation was achieved with the initial linear (elastic) experimental response of the composite. For the 650 °C reference case shown in Fig. 13, a fiber volume fraction of 33% was used in the simulations.

After setting the fiber strengths and fiber volume fraction, the debonding parameters Λ and B were chosen to achieve good correlation between model and experiment. As Fig. 13 shows, the chosen values of $\Lambda = 1.45\times10^{-6}$ MPa^{-1} and $\mathrm{B} = 9$ s provide excellent agreement with the experimental stress-strain curve at 650 °C. The **ECI** model appears to over-predict the composite stiffness decrease associated with the failure of fibers prior to composite failure. Thus the strain to failure is over-predicted in this case. A numerical comparison of the UTS and strain to failure for this case (and all other simulated cases) is given in Table 4, while bar charts comparing the values are given in Fig. 14 and Fig. 15.

Fig. 13 also shows the **ECI** model prediction for a nominally 35% SCS-6/TIMETAL 21S composite at 23 °C. By matching the initial stress-strain response of the experimental curve shown, a more accurate fiber volume fraction of 32% was determined for this case. Thus, using $\mathrm{B}_{\text{ref}} = 9$ s and $V_f^{\text{ref}} = 33\%$ in conjunction with eqn (18) yields $\mathrm{B} = 8.73$ s for this case. Note that the global strain rate for both this and the reference case was 1.67×10^{-4} s^{-1}. As Fig. 13 shows, the predicted UTS and strain to failure agree quite well with experiment and are underpredicted by only 1.1% and 1.2%, respectively (with respect to the average experimental values). However, the stress is over-predicted by the model beyond approximately 0.6% strain. It appears that the onset of yielding is delayed in the simulation compared to experiment, indicating that the residual stress state predicted by **MAC/GMC** in this analysis is somewhat inaccurate (see Goldberg and Arnold, 1999). This may be due to the use of temperature dependent fiber properties. Were the composite yielding behavior better simulated by **MAC/GMC**, the **ECI** model would over-predict the stiffness decrease prior to failure as well as the strain to failure, much as it did in the 650 °C case.

Also plotted in Fig. 13 are predictions made using the Curtin effective fiber breakage model in conjunction with **MAC/GMC** for the tensile response of the nominally 35% SCS-6/TIMETAL 21S, and predictions for the case in which no fiber failure is permitted. The Curtin model was included in **MAC/GMC** for a simple repeating unit cell like that shown in Fig. 6 by simply reducing the fiber elastic modulus according to eqn (7) during simulated longitudinal tensile loading. Furthermore, global

system	**Vf (%)**	**Temp. (°C)**	**Experiment**		**ECI Model**		**Curtin Effective Model**	
			UTS	**STF**	**UTS**	**STF**	**UTS**	**STF**
SCS-6/TIMETAL 21S	35	23	1958	1.127	1929	1.114	2102	1.214
			1943	1.128				
		650	1250	0.909	1249*	0.948*	1431	1.072
SCS-6/TIMETAL 21S	22	650	887	0.891	886	0.956	1029	1.086
SCS-9/TIMETAL 21S	24	23	1395	1.029	1388	1.004	1642	1.266
			1432	1.031				
		480	1156	0.912	1117	1.012	1414	1.138
			1253	1.086				
		650	760	0.788	707	0.784	978	1.07

Table 4. Comparison of experimental and predicted longitudinal ultimate tensile strength (**UTS**) data (MPa) and strain to failure (**STF**) data (%) for SiC/TIMETAL 21S composites. * indicates that experimental data was used for characterization purposes.

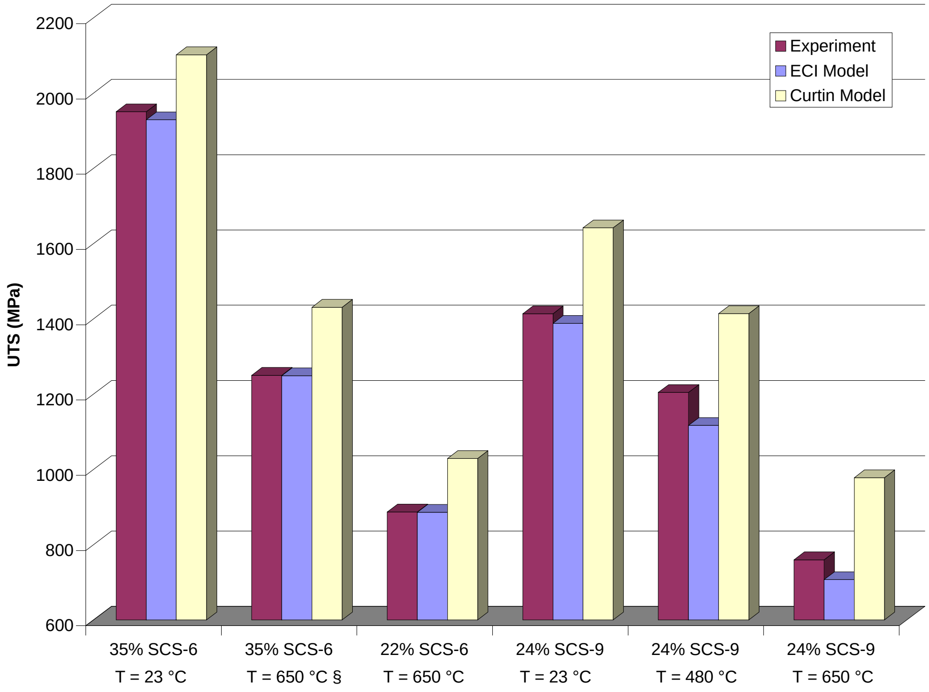

Fig. 14. Comparison of average experimental and predicted longitudinal ultimate tensile strength (**UTS**) data for SCS-6/ and SCS-9/TIMETAL 21S composites. § indicates that experimental data from the case was used for ECI model correlation.

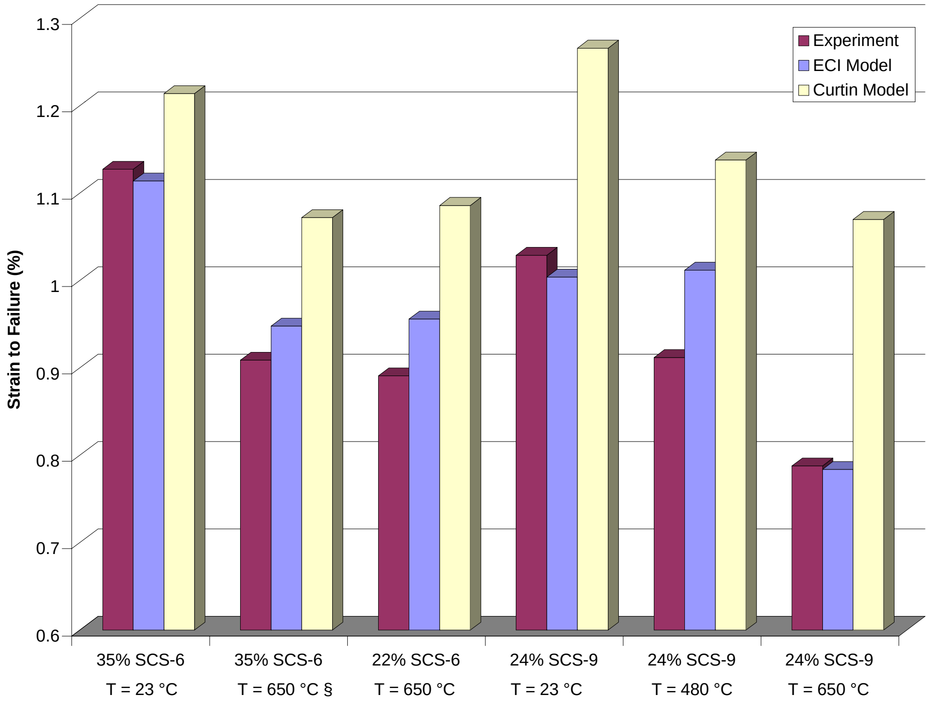

Fig. 15. Comparison of average experimental and predicted longitudinal strain to failure data for SCS-6/ and SCS-9/TIMETAL 21S composites. § indicates that experimental data from the case was used for ECI model correlation.

composite failure was considered to occur when the longitudinal mechanical strain in the fiber satisfied eqn (8). The simple unit cell geometric representation may be employed because the Curtin model treats all fibers in the composite as a single effective fiber. As in the case of the **ECI** model, actual fiber volume fractions of 33% and 32% were used for the Curtin model simulation for the 650 °C and 23 °C temperatures, respectively.

Fig. 13, Fig. 14, and Fig. 15 show that the Curtin model significantly over-predicts both the composite UTS (over-predicted by an average of 11.2%) and strain to failure (over-predicted by an average of 12.8%) (see also Table 4). The decrease in the composite stiffness prior to failure is also much less pronounced than in the case of the **ECI** model predictions, allowing the predicted stress-strain curve to diverge only slightly from the case with no fiber failure. The reason for the inaccuracy of the Curtin model for the current application can be easily understood by examining the classic rule of mixtures approximation for the longitudinal stiffness of a continuous composite wherein,

$$E_c = V_f\, E_f + \left(1 - V_f\right) E_m, \tag{19}$$

with E_f, E_m, and E_c being the elastic moduli of the fiber, matrix, and composite, respectively. The Curtin model simulates the effects of breaking fibers on the composite behavior by progressively decreasing E_f via the effective fiber modulus given by eqn (7). Clearly, this effect manifests itself in the composite stiffness through the first term on the right hand side of eqn (19). The Curtin model will thus be most effective when this first term dominates; that is, for high fiber volume fractions or when the fiber's elastic modulus dominates, e.g., in PMC applications (for which it was originally designed). In MMCs like SCS-6/TIMETAL 21S, this is not the case. The fiber volume fraction is usually low, and the elastic modulus of the matrix, while smaller than the fiber elastic modulus, is still significant. In the present SCS-6/TIMETAL 21S case, the fiber volume fraction is 32% or 33%, while (at room temperature) $E_f/E_m = 3.4$. Thus the two terms on the right hand side of eqn (19) are different by only a factor of 1.6, and the composite stiffness decrease provided by the decreasing effective fiber modulus in the Curtin model is only slight. The Curtin composite failure criterion is linked to the effective fiber modulus since it dictates the point at which the maximum fiber stress will occur (see Section 4.1). Thus the ineffectuality of the decreasing effective fiber modulus associated with the Curtin model also results in the over-prediction of the composite UTS and strain to failure for MMCs. For PMCs, in which the two terms on the right hand side of eqn (19) are typically different by a factor of approximately 100, the Curtin model would clearly perform better.

Alternatively, the **ECI** model, simulates actual failure of individual fibers in the repeating unit cell, which then unload from the failure stress. This, in effect, progressively decreases the fiber volume fraction of the composite as the fibers break and are unable to support load. Consequently, the failure effects are manifested in both terms on the right hand side of eqn (19), and lead to significantly greater (and more realistic) composite stiffness decrease prior to failure. Thus the approach represented by the **ECI** model appears to be better suited than the Curtin model for simulating the longitudinal behavior of MMCs.

6.1.2 Cyclic Response

Differences between the **ECI** and Curtin models are further highlighted by comparing the predicted longitudinal cyclic response provided by the two approaches. Fig. 16 provides such a comparison for the case of 33% SCS-6/TIMETAL 21S at 650 °C (whose monotonic response is given in Fig. 13). Also included in this figure is the predicted response of the composite with no fiber breakage or damage. Near the maximum stress of the first cycle, the stress-strain curve associated with the Curtin model diverges only slightly from the undamaged composite stress-strain curve. As illustrated previously, the stiffness decrease (during the first cycle) associated with the **ECI** model is significantly greater than that associated with the Curtin model. Upon unloading from the maximum stress of the first cycle, the stress in the fiber naturally begins to decrease, as does the stiffness degradation associated with

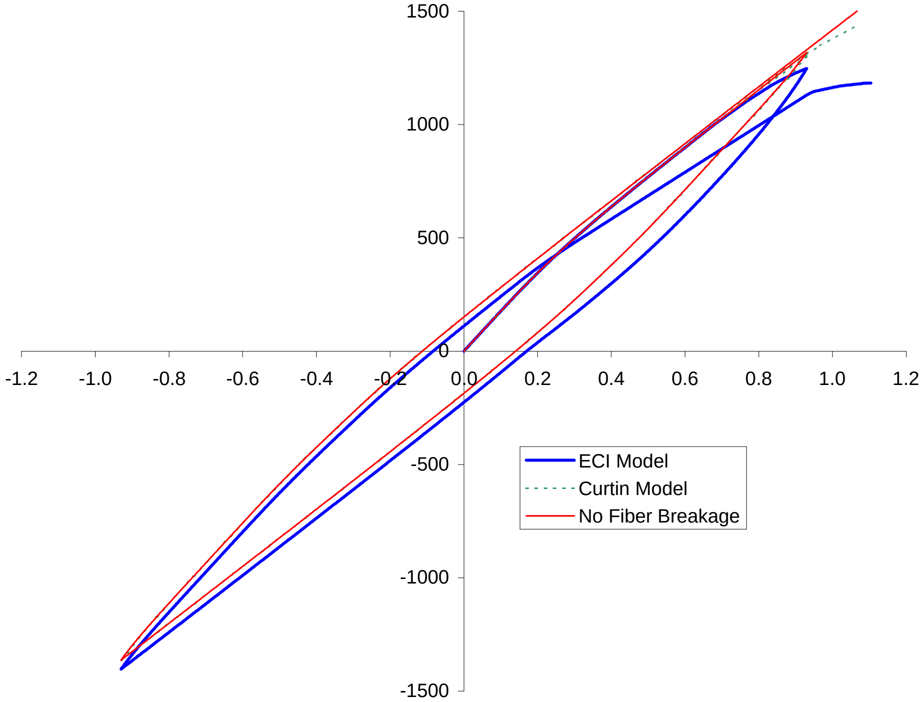

Fig. 16. Comparison of the simulated longitudinal cyclic tensile response of 33% SCS6/TIMETAL 21S obtained via the **ECI** and Curtin models. $\dot{\varepsilon} = 1.67 \times 10^{-4}$ s^{-1}.

the Curtin model (see eqn (7)). Thus, as the stress in the fiber decreases, the damage in the Curtin model fiber is, in effect, healing. Since little damage has occurred in the Curtin model, this healing occurs quickly, and most of the Curtin unloading stress-strain curve follows the unloading curve associated with the undamaged prediction closely. In contrast, the fibers that have broken during tensile loading (4 of 28 fibers) when using the **ECI** model remain broken upon unloading, giving the composite unloading curve a more matrix-like appearance than that of the Curtin model. In the ECI model, the fibers that were broken upon loading heal when the local stress in the fiber becomes negative. This healing manifests itself as a slight jog in the **ECI** model unloading curve in Fig. 16 near the horizontal axis. While in compression, both models treat the fibers as completely healed, and the predicted curves for the composite are very similar (although offset). When the fiber once again goes into tension during the second cycle, the entire process associated with damaging the Curtin fiber begins again; the fiber behaves as (initially) completely undamaged. The Curtin model predicted second-cycle stress-strain curve follows the Curtin monotonic curve closely (see Fig. 13), and predicted failure occurs at a slightly higher stress (1442 MPa vs. 1431 MPa). Alternatively, in the **ECI** model, the previously broken fibers remain broken and are unable to support tensile stress. The result is a much more compliant response during the second tensile loading cycle and ultimately the predicted failure is at a significantly lower stress compared to the monotonic case (1183 MPa compared to 1249 MPa) as shown in Fig. 13. Experimental verification of this behavior will be the subject of future work.

6.2 Nominally 22% Volume Fraction SCS-6/TIMETAL 21S

Fig. 17 shows the experimental and **predicted** longitudinal tensile response for nominally 22% SCS-6/TIMETAL 21S at 650 °C and 23 °C. Note that the global strain rate has changed from the reference value of 1.67×10^{-4} s^{-1} to 10^{-4} s^{-1}, and that the actual fiber volume fractions employed in the simulations are 22% for 650 °C and 20 % for 23 °C. Thus, according to eqn (18), the values $\mathrm{B} = 10$ s

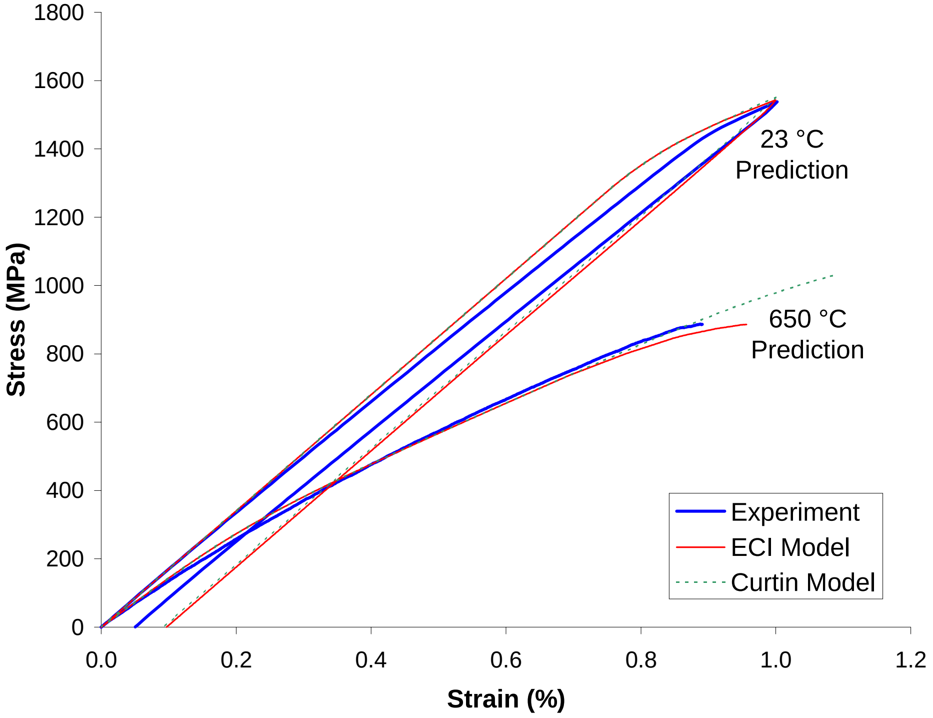

Fig. 17. Comparison of the simulated and experimental longitudinal tensile response of nominally 22% SCS-6/TIMETAL 21S. $\dot{\varepsilon} = 10^{-4}$ s^{-1}.

and $\mathrm{B} = 9.09$ s were used in the **ECI** model for 650 °C and 23 °C, respectively (using the previously defined baseline case). As in the previous cases, at 650 °C, the **ECI** model over-predicts the composite stiffness decrease somewhat prior to failure, leading to an over-prediction of the composite strain to failure (by 7.3%). However, the **ECI** model still provided an accurate prediction of the composite UTS (which is underpredicted by 0.1%) (see Table 4 and Fig. 15); whereas the Curtin model again significantly over-predicted the composite UTS (by 16.0%) and strain to failure (by 21.9%) at this temperature. The 23 °C tensile test was not taken to failure, but rather unloaded after an applied longitudinal strain of 1%. As in the previous room temperature case, the stress associated with the deformation response of the composite was overpredicted, indicating inaccuracies in the simulated residual stress field, most likely due to inaccuracy in the matrix and fiber constituent representations. Little fiber damage (i.e., fiber breakage) occurred in the simulations by the time the global loading was reversed, consequently the predictions of both the Curtin and **ECI** models are nearly coincident.

*6.3 Nominally 24% Volume Fraction **SCS-9**/TIMETAL 21S*

In order to investigate the ability of the new **ECI** model to capture the discrete breakage behavior of fibers other than the SCS-6 (without resorting to re-calibrating the debond parameters), simulations were performed for the longitudinal tensile behavior of nominally 24% **SCS-9**/TIMETAL 21S. The SCS-9 SiC fiber has a smaller diameter than the SCS-6 SiC fiber, and it is somewhat weaker as well. As before, the **GMC-TP** repeating unit cell containing 28 fibers (see Fig. 8) was employed. The actual and simulated fiber strength histograms for the SCS-9 fiber are given in Fig. 18. The temperature-independent elastic properties employed for the SCS-9 were given in Section 3.1. The reference debonding parameters obtained via correlation with experiment for the SCS-6/TIMETAL 21S system were used for the SCS-9/TIMETAL 21S system. In addition, simulations for this system were performed

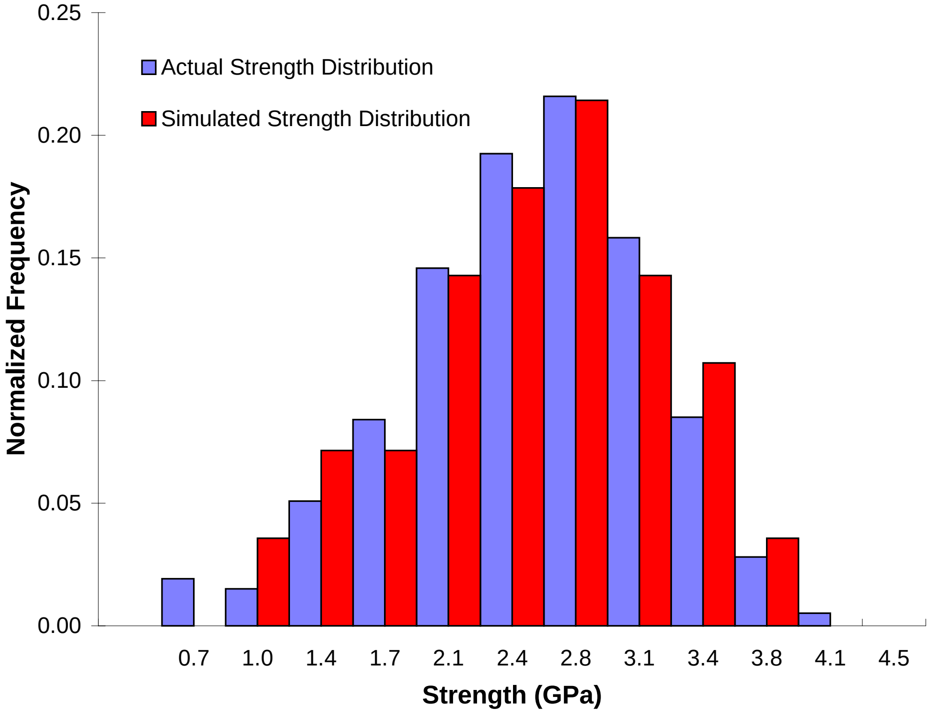

Fig. 18. Actual and simulated SCS-9 fiber strength histograms.

using the Curtin model. The Curtin model parameters employed are: $D = 76.2$ μm; $L_0 = 25.4$ mm; $\sigma_0 = 2520$ MPa; $m = 5.5$; $\tau_0 = 48$ MPa (Grant and Kumnick, 1991). Note that only D, σ_0, and m are modified, and these are directly obtainable from vendor data. Finally, data on the temperature dependence of the SCS-9 fiber were unavailable so the same fiber strength distribution was used for all temperatures (see Fig. 18).

The model and experimental results for the nominally 24% volume fraction SCS-9/TIMETAL 21S are shown in Fig. 19. The model results at all three temperatures are purely predictive as no model parameters were recalibrated specifically for the simulations shown; parameters were modified based on vendor-supplied data only. The actual fiber volume fractions employed in the simulations are 26%, 24%, and 24% for 650 °C, 480 °C, and 23 °C, respectively, which correspond to the adjusted nominal fiber volume fractions of the experimental specimens. The applied strain rate was 1.67×10^{-4} s^{-1}, thus, according to eqn (18), the employed B values are 7.09 s, 6.55 s, and 6.55 s, respectively.

Clearly, the **ECI** model predictions for this SCS-9 system are somewhat less accurate than those obtained for the SCS-6 system. In particular, the composite stiffness decrease prior to failure has been over-predicted to a greater extent. In the case of the SCS-6 system, this over-prediction lead to an over-prediction of the composite strain to failure (see Fig. 15) whereas for the SCS-9 system it leads to an under-prediction of the composite UTS (see Fig. 14). On average, the ECI model underpredicts the UTS of the SCS-9/TIMETAL 21S composite by 5.4% and its strain to failure by 1.4%. However, the discrepancy between the Curtin model predictions and experiment has increased as well, where the Curtin model now drastically over-predicts the composite UTS, strain to failure, and near-failure deformation. On average, the Curtin model over-predicts the composite UTS by 20.8% and the strain to failure by 24.2%. Alternatively, although the **ECI** model predictions are less accurate than before, they are still in reasonably good agreement with the experimental stress-strain curves. Note, some of the inaccuracy displayed by both models may be attributable to the fact that the thermo-mechanical properties of the SCS-9 fiber are not as well established as those of the SCS-6 fiber.

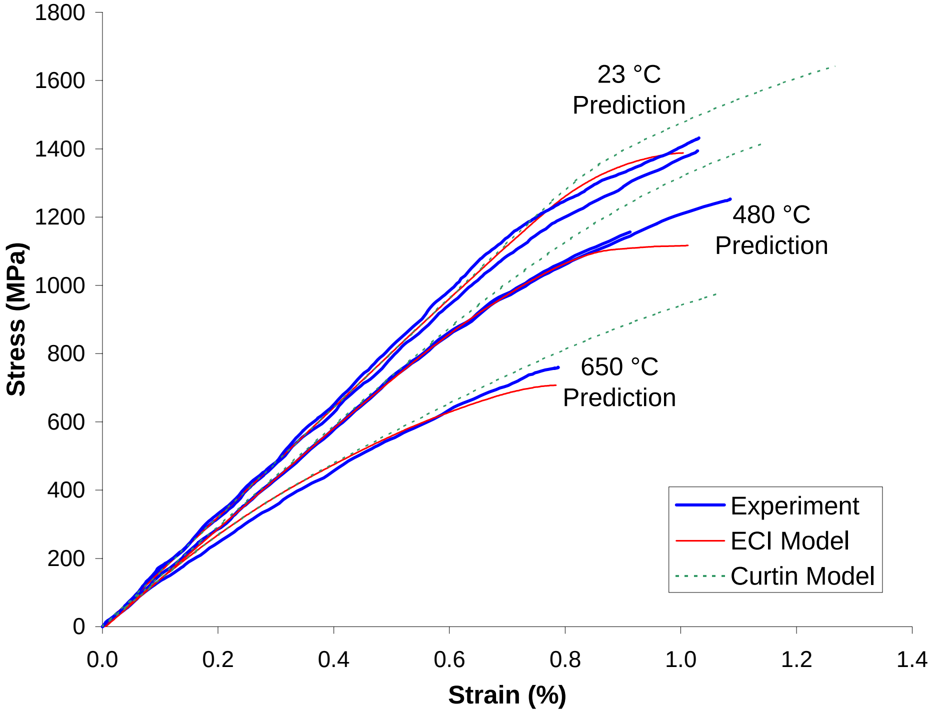

Fig. 19. Comparison of the simulated and experimental longitudinal tensile response of nominally 24% SCS-9/TIMETAL 21S. $\dot{\varepsilon} = 1.67 \times 10^{-4} \mathrm{s}^{-1}$.

7. Summary/Conclusions

A new local evolving compliant interface (**ECI**) failure/debonding model has been developed, incorporated into NASA Glenn's Micromechanics Analysis Code with Generalized Method of Cells (**MAC/GMC**), and applied to simulate the longitudinal tensile deformation and failure behavior of TIMETAL 21S matrix composites. The **ECI** model is based on an existing compliant interface model, but unlike its predecessor (the constant compliant interface, **CCI**, model) the **ECI** model allows the stress in a particular fiber to unload after the fiber has failed, thereby allowing improved simulation of the global manifestation of the effects of the actual local fiber fragmentation, debonding, and shear-lag stress transfer process. Thanks to recent advances that have increased the computational efficiency of **MAC/GMC**, detailed micro level simulations, in which a unit cell representation comprising 28 individual fibers, were enabled. These 28 fibers were assigned strengths based on vendor-supplied fiber strength histograms (along with strength temperature dependence data), allowing accurate simulation of fiber breakage in the composite during longitudinal tensile loading.

A procedure was outlined for characterizing the **ECI** model parameters based on a single, elevated temperature, experimental stress-strain curve. Based on parameters chosen to obtain good correlation with this curve, the parameters can be changed to allow the application of the model to different fiber volume fractions and strain rates. Predictions were made for the longitudinal tensile behavior of TIMETAL 21S reinforced with SCS-6 and SCS-9 fibers with different fiber volume fractions, with different applied strain rates, and at different temperatures. In general, the model predictions exhibited good agreement with experimental tensile deformation and failure data. The **ECI** model was shown to yield more accurate predictions than the Curtin effective fiber breakage model that has been applied to titanium matrix composites in the past. The main weakness of the new model with respect to its application to longitudinal tension involves over-prediction of the composite compliance prior to failure. This leads to some inaccuracy in either the predicted strain to failure of the composite (for the

SCS-6 system) or the predicted UTS of the composite (for the SCS-9 system). However, as Table 4, Fig. 14, and Fig. 15 illustrate, if the **ECI** model prediction of either the composite UTS or strain to failure is inaccurate, the other quantity typically exhibits good agreement with experiment.

References

Aboudi, J. (1988) "Constitutive Equations for Elastoplastic Composites with Imperfect Bonding" *International Journal of Plasticity*. Vol. 4, pp. 103-125.

Aboudi, J. (1991) *Micromechanics of Composite Materials: A Unified Micromechanical Approach*. Elsevier, Amsterdam.

Aboudi, J. (1995) "Micromechanical Analysis of Thermo-Inelastic Multiphase Short-Fiber Composites" *Composites Engineering*. Vol. 5, no. 7, pp. 839-850.

Achenbach, J.D. and Zhu, H. (1989) "Effect of Interfacial Zone on Mechanical Behavior and Failure of Fiber-Reinforced Composites" *Journal of the Mechanics and Physics of Solids*. Vol. 37, No. 3, pp. 381-393.

Arnold, S.M., Bednarcyk, B.A., Wilt, T.E., and Trowbridge, D. (1999) "**MAC/GMC** Users Guide: Version 3.0" *NASA/TM-1999-209070*.

Arnold, S.M. and Saleeb, A.F., (1994) "On the Thermodynamic Framework of Generalized Coupled Thermoelastic-Viscoplastic-Damage Modeling," *International Journal of Plasticity*, Vol. 10, No. 3, pp. 263-278.

Arnold, S.M., Saleeb, A.F., and Castelli, M.G., (1996a) "A Fully Associative, Nonisothermal, Nonlinear Kinematic, Unified Viscoplastic Model for Titanium Alloys," in *Thermo-Mechanical Fatigue Behavior of Materials: Second Volume*. M.J. Verrilli and M.G. Castelli (eds.), ASTM STP-1263, American Society for Testing and Materials, Philadelphia, pp. 146-173.

Arnold, S.M., Saleeb, A.F., and Castelli, M.G., (1996b) "A Fully Associative, Nonlinear Kinematic, Unified Viscoplastic Model for Titanium Based Matrices," in *Life Prediction Methodology for Titanium Matrix Composites*. W.S. Johnson, J.M. Larsen, and B.N. Cox (eds.), ASTM STP-1253, American Society for Testing and Materials, Philadelphia, pp. 231-256.

Bednarcyk, B.A. and Pindera, M.-J. (2000) "Inelastic Response of a Woven Carbon/Copper Composite – Part II: Micromechanics Model" *Journal of Composite Materials*, Vol. 34, No. 4, pp. 299-331. See also *NASA CR-204153*, 1997.

Bowman, C.L. (1999) "Experimentation and Analysis of Mechanical Behavior Modification of Titanium Matrix Composites Through Controlled Fiber Placement" Ph.D. Dissertation, Case Western Reserve University.

Brindley, P.K. and Draper, S.L. (1993) "Failure Mechanisms of 0° and 90° SiC/Ti-24Al-11Nb Composites Under Various Loading Conditions" *Structural Intermetalics*. R. Darolia et al eds., The Minerals, Metals & Materials Society, pp. 727-737.

Chan, K.S., Bodner, S.R., and Lindholm, U.S., (1988) "Phenomenological Modeling of Hardening and Thermal Recovery in Metals," *Journal of Engineering Materials and Technology*, Vol. 110, pp. 1-8.

Chan, K.S. and Lindholm, U.S., (1990) "Inelastic Deformation Under Nonisothermal Loading," *Journal of Engineering Materials and Technology*, Vol. 112, pp. 15-25.

Curtin, W.A. (1991) "Theory of Mechanical Properties of Ceramic-Matrix Composites" *Journal of the American Ceramics Society*. Vol. 74, no. 11, pp. 2837-2845.

Curtin, W.A. (1993) "Ultimate Strengths of Fibre-Reinforced Ceramics and Metals" *Composites*. Vol. 24, no. 2, pp. 98-102.

Goldberg, R. K. and Arnold, S. M. (1999) "A Study of Influencing Factors on the Tensile Response of a Titanium Matrix Composite With Weak Interfacial Bonding", *NASA/TM-1999-209798*.

Grant, W.F. and Kumnick, A.J. (1991) "Development of a 3-Mil Silicon Carbide Fiber for Titanium Matrix Composites" presented at the Third International Aerospace Planes Conference, Orlando, FL.

Harlow, D.G. and Phoenix, S.L. (1978a) "The Chain-of-Bundles Probability Model for the Strength of Fibrous Materials I: Analysis and Conjectures" *Journal of Composite Materials*. Vol. 12, pp. 195-214.

Harlow, D.G. and Phoenix, S.L. (1978b) "The Chain-of-Bundles Probability Model for the Strength of Fibrous Materials II: A Numerical Study of Convergence" *Journal of Composite Materials*. Vol. 12, pp. 314-334.

Kroupa, J.L. (1993) "Implementation of a Nonisothermal Unified Inelastic-Strain Theory Into ADINA6.0 for a Titanium Alloy- User Guide," Wright Laboratory WL-TR-93-4005, University of Dayton, Dayton, OH.

Mall, S., Fecke, T., and Foringer, M.A. (1998) "Introduction" in *Titanium Matrix Composites Mechanical Behavior*. S. Mall and T. Nicholas, Eds., Technomic Publishing Co., Lancaster, PA, pp. 1-22.

Neu, R.W. (1993) "Nonisothermal Material Parameters For the Bodner-Partom Model" MD-vol.43, Material Parameter Estimation for Modern Constitutive Equations, L.A. Betram, S.B. Brown, and A.D. Freed, Eds., ASME Book No. H00848.

Nicholas, T. and Ahmad, J. (1994) "Modeling Fiber Breakage in a Metal-Matrix Composite" *Composites Science and Technology*. Vol. 52, pp. 29-38.

Pindera, M.-J. and Bednarcyk, B.A. (1999) "An Efficient Implementation of the Generalized Method of Cells for Unidirectional, Multi-Phased Composites with Complex Microstructures" *Composites Part B*. Vol. 30, no. 1, pp. 87-105.

Reifsnider, K.L. and Highsmith, A. (1982) "The Relationship of Stiffness Changes in Composite Laminates to Fracture-Related Damage Mechanisms" in *Fracture of Composite Materials*. G.C. Sin and V.P. Tamuzs (eds.), Martinus Nijhoff Publishers, The Hague, pp. 279-290.

Steif, P.S. (1984) "Stiffness Reduction Due to Fiber Breakage" *Journal of Composite Materials*. Vol. 17, pp. 153-172.

Stumpf, H. and Schwartz, P. (1993) "A Monte Carlo Simulation of the Stress-Rupture of Seven-Fiber Microcomposites" *Composites Science and Technology*. Vol. 49, pp. 251-263.

Walls, D., Bao, G., and Zok, F. (1991) "Effects of Fiber Failure on Fatigue Cracking in a Ti/SiC Composite" *Scripta Metallurgica et Materialia*, Vol. 25, pp. 911-916.

Weber, C.H., Chen, X., Connell, S.J., and Zok, F.W. (1994) "On the Tensile Properties of a Fiber Reinforced Titanium Matrix Composite-I. Unnotched Behavior" *Acta Metallurgica et Materiala*. Vol. 42, No. 10, pp. 3443-3450.

Wilt, T.E. and Arnold, S.M. (1996) "Micromechanics Analysis Code (MAC) User Guide: Version 2.0, *NASA TM-107290*.

REPORT DOCUMENTATION PAGE

Form Approved
OMB No. 0704-0188

Public reporting burden for this collection of information is estimated to average 1 hour per response, including the time for reviewing instructions, searching existing data sources, gathering and maintaining the data needed, and completing and reviewing the collection of information. Send comments regarding this burden estimate or any other aspect of this collection of information, including suggestions for reducing this burden, to Washington Headquarters Services, Directorate for Information Operations and Reports, 1215 Jefferson Davis Highway, Suite 1204, Arlington, VA 22202-4302, and to the Office of Management and Budget, Paperwork Reduction Project (0704-0188), Washington, DC 20503.

1. AGENCY USE ONLY (*Leave blank*)	**2. REPORT DATE** May 2000	**3. REPORT TYPE AND DATES COVERED** Technical Memorandum

4. TITLE AND SUBTITLE A New Local Failure Model With Application to the Longitudinal Tensile Behavior of Continuously Reinforced Titanium Composites	**5. FUNDING NUMBERS** WU–242–23–52–00
6. AUTHOR(S) Brett A. Bednarcyk and Steven M. Arnold	
7. PERFORMING ORGANIZATION NAME(S) AND ADDRESS(ES) National Aeronautics and Space Administration John H. Glenn Research Center at Lewis Field Cleveland, Ohio 44135–3191	**8. PERFORMING ORGANIZATION REPORT NUMBER** E–12224
9. SPONSORING/MONITORING AGENCY NAME(S) AND ADDRESS(ES) National Aeronautics and Space Administration Washington, DC 20546–0001	**10. SPONSORING/MONITORING AGENCY REPORT NUMBER** NASA TM—2000-210027

11. SUPPLEMENTARY NOTES

Brett A. Bednarcyk, Ohio Aerospace Institute, 22800 Cedar Point Road, Brook Park, Ohio 44142 (work funded under NASA contract NCC3–3650); and Steven M. Arnold, NASA Glenn Research Center. Responsible person, Steven M. Arnold, organization code 5920, (216) 433–3334.

12a. DISTRIBUTION/AVAILABILITY STATEMENT Unclassified - Unlimited Subject Categories: 24 and 39 Distribution: Nonstandard This publication is available from the NASA Center for AeroSpace Information, (301) 621–0390.	**12b. DISTRIBUTION CODE**

13. ABSTRACT *(Maximum 200 words)*

A new model for local fiber failures in composite materials loaded longitudinally is presented. In developing the model, the goal was to account for the effects of fiber breakage on the global response of a composite in a relatively simple and efficient manner. Towards this end, the model includes the important feature of local stress unloading, even as global loading of the composite continues. The model has been incorporated into NASA Glenn's Micromechanics Analysis Code with Generalized Method of Cells (MAC/GMC) and was employed to simulate the longitudinal tensile deformation and failure behavior of several silicon carbide fiber/titanium matrix (SiC/Ti) composites. The model is shown to be quite realistic and capable of accurate predictions for various temperatures, fiber volume fractions, and fiber diameters. Furthermore, the new model compares favorably to Curtin's (1993) effective fiber breakage model, which has also been incorporated into MAC/GMC.

14. SUBJECT TERMS Composites; Strength; Residual stress; Micromechanics; Elastic; Inelastic; Modeling	**15. NUMBER OF PAGES** 36
	16. PRICE CODE A03

17. SECURITY CLASSIFICATION OF REPORT Unclassified	**18. SECURITY CLASSIFICATION OF THIS PAGE** Unclassified	**19. SECURITY CLASSIFICATION OF ABSTRACT** Unclassified	**20. LIMITATION OF ABSTRACT**

NSN 7540-01-280-5500

Standard Form 298 (Rev. 2-89)
Prescribed by ANSI Std. Z39-18
298-102